

TITLE: Axon arrival times and physical occupancy establish visual projection neuron integration on developing dendrites in the *Drosophila* optic glomeruli.

AUTHOR NAMES AND AFFILIATIONS

Brennan W. McFarland¹, HyoJong Jang^{1#}, Natalie Smolin^{1#}, Bryce W. Hina¹, Michael J. Parisi², Kristen C. Davis², Timothy J. Mosca², Tanja A. Godenschwege³, Aljoscha Nern⁴, Yerbol Z. Kurmangaliyev⁵, Catherine R. von Reyn^{*1,6}

¹ School of Biomedical Engineering, Science and Health Systems, Drexel University, Philadelphia, PA

² Department of Neuroscience, Vickie and Jack Farber Institute of Neuroscience, Thomas Jefferson University, Philadelphia, PA

³ Department of Biological Sciences, Florida Atlantic University, Boca Raton, FL

⁴ Janelia Research Campus, Howard Hughes Medical Institute, Ashburn, VA

⁵ Department of Biology, Brandeis University, Waltham, MA

⁶ Department of Neurobiology and Anatomy, Drexel University College of Medicine, Philadelphia, PA

Equal contribution

*Correspondence: crv33@drexel.edu

1 SUMMARY

2 Behaviorally relevant, higher order representations of an animal's environment are built from the
3 convergence of visual features encoded in the early stages of visual processing. Although
4 developmental mechanisms that generate feature encoding channels in early visual circuits have
5 been uncovered, relatively little is known about the mechanisms that direct feature convergence
6 to enable appropriate integration into downstream circuits. Here we explore the development of a
7 collision detection sensorimotor circuit in *Drosophila melanogaster*, the convergence of visual
8 projection neurons (VPNs) onto the dendrites of a large descending neuron, the giant fiber (GF).
9 We find VPNs encoding different visual features establish their respective territories on GF
10 dendrites through sequential axon arrival during development. Physical occupancy, but not
11 developmental activity, is important to maintain territories. Ablation of one VPN results in the
12 expansion of remaining VPN territories and functional compensation that enables the GF to
13 retain responses to ethologically relevant visual stimuli. GF developmental activity, observed
14 using a pupal electrophysiology preparation, appears after VPN territories are established, and
15 likely contributes to later stages of synapse assembly and refinement. Our data highlight
16 temporal mechanisms for visual feature convergence and promote the GF circuit and the
17 *Drosophila* optic glomeruli, where VPN to GF connectivity resides, as a powerful developmental
18 model for investigating complex wiring programs and developmental plasticity.

19

20 Keywords: Pupal Development, *Drosophila melanogaster*, Giant Fiber, Optic Glomeruli, Neural
21 Activity, Adaptation, Electrophysiology, Visual Projection Neurons, Visual System, Descending
22 Neuron

23

24 INTRODUCTION

25 In a developing brain, the coordinated wiring of multiple inputs onto a neuron and
26 organization of these inputs across a neuron's dendrites establish the computational role for that
27 neuron. Uncovering the mechanisms that assemble and localize multiple inputs is pivotal to
28 understand how inputs are miswired in neurodevelopmental disorders¹⁻³ and how developmental
29 processes attempt to compensate when particular inputs are missing or fail to connect^{4,5}. Across
30 species, we know little about how multiple inputs that converge upon a neuron are wired during
31 development because the underlying circuits are often not well established – we are missing the
32 solution to the wiring program, where all inputs are known and synapse locations are mapped.

33 Here, we capitalize on recent connectome data and functional investigations within the
34 *Drosophila* optic glomeruli, a central brain region where visual feature inputs converge onto
35 sensorimotor circuits⁶⁻¹⁰. Optic glomeruli are the output region for columnar visual projection
36 neurons (VPNs) that are hypothesized to encode visual features^{9,11-14}. VPN dendrites are
37 retinotopically distributed to tile the lobula and the lobula plate of the fly's optic lobes, while
38 fasciculated VPN axons terminate within their respective glomerulus¹¹. Within each glomerulus,
39 VPNS synapse with multiple targets, including descending neurons (DNs) that project axons to
40 the ventral nerve cord (VNC, the fly spinal cord homologue) where they in turn synapse onto
41 interneurons and motoneurons that generate behavioral outputs¹⁵⁻¹⁷. Unlike the *Drosophila*
42 olfactory glomeruli which have a predominantly one to one olfactory receptor neuron to
43 projection neuron mapping¹⁸, each VPN glomerulus is not dedicated to a single DN type.
44 Instead, DN dendrites infiltrate multiple, semi-overlapping subsets of glomeruli^{10,16,19}, essentially
45 assembling VPN features into higher order, behaviorally relevant motor and premotor outputs.

46 How this complex wiring of visual feature inputs onto DNs is established during development is
47 presently unknown.

48 A pair of large DNs called the giant fibers (GFs) receive major input from two VPN types
49 in the optic glomeruli: lobula columnar type 4 (LC4) neurons and lobula plate - lobula columnar
50 type 2 (LPLC2) neurons (Figure 1A)^{6,7,13}. LC4 and LPLC2 encode the angular velocity and
51 angular size of an expanding object, respectively^{6,7}, and enable the GFs to drive a rapid takeoff
52 escape in response to an object approaching on a direct collision course¹⁷. The GF circuit within
53 the optic glomeruli presents an ideal model for developmental investigations. GF connectivity in
54 adult flies has been recently established through electron microscopy, genetic access exists for
55 the GF and its major visual input cell types, and the large GF dendrites within the glomeruli can
56 be resolved and tracked across development^{6,7,20,21}. Additionally, the accessibility of the GF to
57 electrophysiology enables the functional consequences of developmental events to be directly
58 evaluated^{6,7}. GF dendrites are also in close proximity to VPNs that are not synaptic partners in
59 the adult, like lobula plate - lobula columnar type 1 (LPLC1) neurons. This provides an
60 opportunity to investigate developmental interactions with cell types that do or do not select the
61 GF as a synaptic partner.

62 Here, we establish the GF circuit^{6,7,17} as a model for visual feature convergence in a
63 developing nervous system. We screened VPN and GF GAL4 and LexA driver lines for early
64 developmental expression and cell-type specificity. We then used identified driver lines to
65 characterize the timecourse of VPN and GF interactions across metamorphosis that lead to their
66 final organization in the adult. Combining a comprehensive single-cell RNA sequencing
67 (scRNA-seq) atlas of the developing *Drosophila* visual system²², synaptic protein labeling over
68 development, and a novel *ex-plant* electrophysiology preparation that enabled us to record from

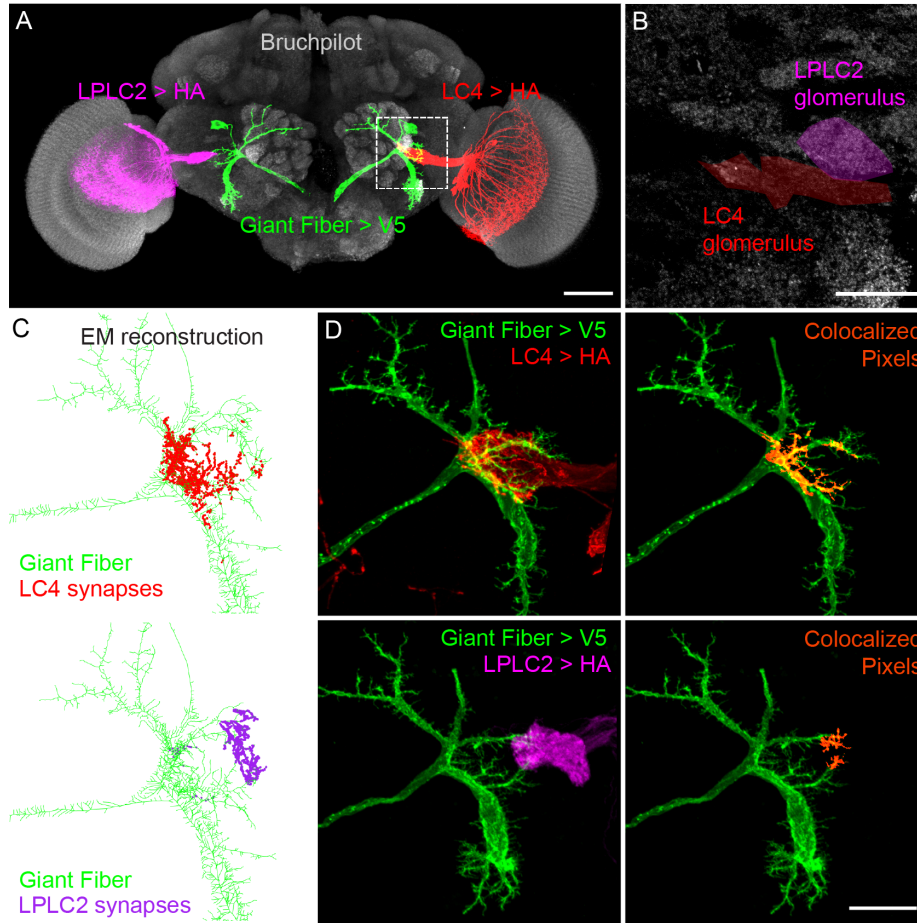
69 the GF at distinct developmental timepoints, we correlated the time course of VPN to GF
70 interactions with the arrival of synaptic machinery and neural activity. To determine how
71 competition shapes VPN synapse organization along GF dendrites, we genetically ablated one
72 VPN cell type (LC4) and investigated both structural and functional compensation from the
73 surviving VPN partner (LPLC2). Our data provide a thorough characterization of the assembly
74 of visual feature convergence onto GF dendrites and establish the optic glomeruli as a genetically
75 and functionally tractable model to uncover mechanisms underlying complex wiring programs.

76

77 **RESULTS**

78 **VPNs are localized to stereotyped regions on GF dendrites**

79 GF dendrites extend into the optic glomeruli in close proximity to multiple VPN cell-
80 types (Figure 1A,B). EM reconstruction of a full adult fly brain (FAFB²⁰) previously revealed
81 that 55 LC4 and 108 LPLC2 neurons connect directly onto GF optic glomeruli dendrites,
82 contributing 2,442 and 1,366 synapses, respectively⁷. VPN synapses segregate across the medial-
83 lateral axis, with LC4 predominantly localized to medial, and LPLC2 to lateral, dendritic
84 regions⁷. To investigate stereotypy in VPN to GF connectivity, we utilized a second EM dataset
85 of a *Drosophila* hemibrain^{21,23}. In this EM reconstruction, we found LC4 (71/71) and LPLC2
86 (85/85) neurons established 2,290 and 1,443 synapses onto the GF optic glomeruli dendrites,
87 respectively (Figure 1C). We confirmed LC4 and LPLC2 synapses segregate along the medial-
88 lateral axis, with only 2/85 LPLC2 neurons making synapses in predominantly LC4 occupied
89 medial areas.



90

91 **Figure 1. LC4 and LPLC2 occupy distinct regions on GF dendrites**

92 (A) GF (green), LPLC2 (magenta, one hemisphere), and LC4 (red, one hemisphere) maximum
93 intensity projections superimposed over neuropil label Bruchpilot (Brp, gray) Scale bar, 50 μ m.
94 (B) Optic glomeruli as identified by Brp labeling with the LPLC2 (magenta) and LC4 (red)
95 glomeruli highlighted. Maximum intensity projection of a substack located within the dashed
96 box in (A). Scale bar, 20 μ m.
97 (C) *Drosophila* hemibrain EM reconstruction of GF (green) with colored dots indicating
98 synapses from LC4 (red, top) and LPLC2 (magenta, bottom).
99 (D) (Left) Maximum intensity projections of dual labeled GF and VPNs. (Right) Colocalized
100 pixels (orange) between GF and respective VPNs superimposed over GF maximum intensity
101 projections. Scale bar, 20 μ m.
102

103 Since existing EM data only represent connectivity within two fly brains, we further
104 investigated localization stereotypy by examining contacts between GF and VPN membranes
105 across multiple adult flies. We used split-GAL4 driver lines that selectively labeled LC4 (*LC4_4-*
106 *split-GAL4*, generated for this paper) or LPLC2 (*LPLC2-split-GAL4*)¹¹, and simultaneously

107 labeled the GF with a LexA line (*GF_I-LexA*)²⁴ (Figure 1D, left). As a proxy for membrane
108 contacts, we performed intensity-based thresholding on each cell-type of interest to generate
109 representative masks, and then visualized colocalized regions along GF dendrites (Figure 1D,
110 right). We consistently observed LC4 contacts on the most medial regions of the GF optic
111 glomeruli dendrites and LPLC2 contacts on the most lateral regions. We also found on occasion
112 (4/17 brain hemispheres), as seen in the hemibrain dataset, a small subset of LPLC2 axons
113 extending into the most medial regions on the GF (Supplemental Figure 1, arrow)²¹. These data
114 suggest that LC4 and LPLC2 consistently segregate to stereotyped regions along the medial-
115 lateral axis with rare exceptions.

116 We used the same approach to assess the projections of LPLC1 (*LPLC1_I-split-GAL4*)¹¹,
117 a cell-type adjacent to LC4 and LPLC2 that does not synapse directly with the GF⁷. As expected,
118 no synapses were identified in the hemibrain EM dataset (Supplemental Figure 2) and no
119 membrane contacts were observed between GF and LPLC1 across all adult flies imaged with
120 confocal microscopy (Supplemental Figure 2). We additionally employed GFP reconstitution
121 across synaptic partners (GRASP)^{25,26} to visualize contacts between adjacent membranes and
122 observed GFP expression between GF and LC4/LPLC2 in their respective medial/lateral
123 locations, but not between GF and LPLC1 (Supplemental Figure 3).

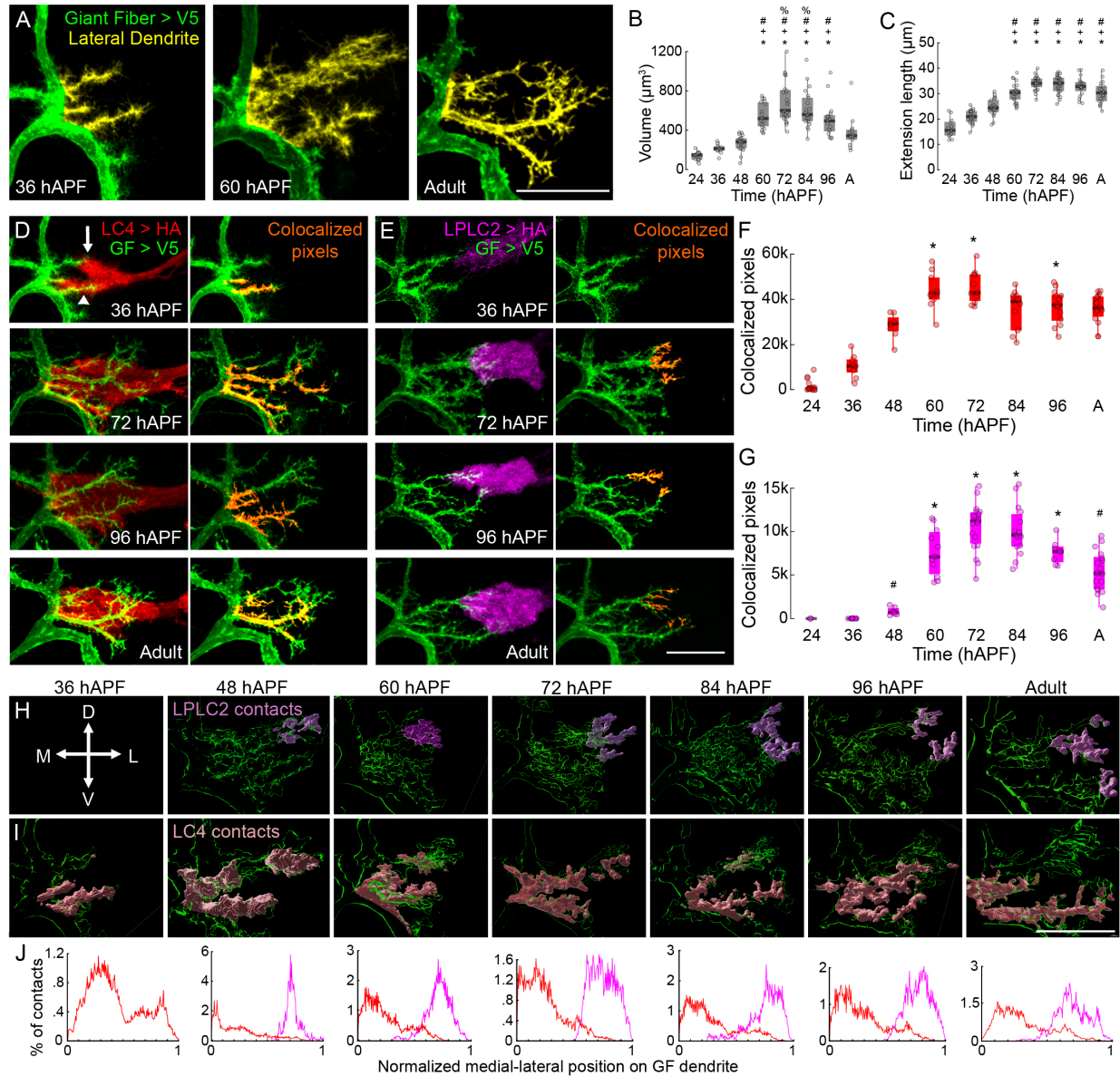
124

125 **GF lateral dendrites extend, elaborate, and then refine across pupal stages**

126 Following our detailed anatomical characterization, we sought to determine how the
127 precise VPN localization along GF dendrites arises across development. Prior developmental
128 investigations into the GF have focused on axonal wiring with respect to postsynaptic
129 interneuron and motor neuron partners in the ventral nerve cord (VNC)²⁷⁻³². However, little is

130 known about how GF dendrites develop in the central brain³³. The GF is born during embryonic
131 stages but does not generate neurites until the third instar larval stage²⁷. To track the GF at these
132 early timepoints, we used the *GF_I-LexA* line that labels the GF starting in late larval stages
133 (Supplemental Figure 4) and dissected pupae in 12-hour increments over metamorphosis, a
134 period marked as the time between pupa formation and eclosion.

135 Across development, we tracked the complexity and size of GF optic glomeruli dendrites
136 by quantifying their volume (Figure 2A,B) and the length of the maximum dendrite extension
137 along the medial-lateral axis (Figure 2A,C). In the early stages of metamorphosis, 24-48 hours
138 after pupa formation (hAPF), the GF exhibited numerous filopodia, long thin protrusions without
139 a bulbous head, and arbor complexity increased with the GF projecting between 3.1 ± 1.0
140 primary dendrites laterally (Figure 2A,B). During the middle stages of metamorphosis, from 48
141 hAPF to 60 hAPF, the GF dendrites had the largest increase in their medial-lateral extent (Figure
142 2C), followed by a peak in the overall volume and extension length at 72 hAPF (Figure 2A-C).
143 During this time, filopodia were still present, but visibly shorter than in the first half of
144 metamorphosis. In the final stages of metamorphosis from 72 hAPF to eclosion, the volume of
145 GF dendrites significantly decreased (Figure 2A-C), while the medial-lateral length was
146 maintained. Filopodia were no longer obvious, and branches appeared less complex and began to
147 resemble their adult morphology.



148

149 **Figure 2. LC4 and LPLC2 territories on GF dendrites are established early in development**

150 (A) Maximum intensity projections of GF (green) 36 hAPF (left), 60 hAPF (middle), and in
 151 in adult (right) with the VPN dendritic region highlighted in yellow at distinct developmental
 152 stages. Scale bar, 20µm.

153 (B) Quantification GF lateral dendrite volume from (A). Unpaired Kruskal-Wallis test ($p = 1.339$
 154 $\times 10^{-18}$), Tukey-Kramer multiple comparison test post hoc, * = $p < .05$ as compared to 24 hAPF,
 155 + = $p < .05$ as compared to 36 hAPF, # = $p < .05$ as compared to 48 hAPF, and % = $p < .05$ as
 156 compared to adult. $N \geq 13$ hemibrains from ≥ 10 flies.

157 (C) Quantification of maximum dendrite extension length across the medial-lateral axis.
 158 Unpaired Kruskal-Wallis test ($p = 2.072 \times 10^{-12}$), Tukey-Kramer multiple comparison test post
 159 hoc, * = $p < .05$ compared to 24 hAPF, + = $p < .05$ compared to 36 hAPF, # = $p < .05$ compared
 160 to 48 hAPF.

161 **(D,E)** Left, maximum intensity projections of GF (green) with respect to LC4 (red, D), and
162 LPLC2 (magenta, E) axonal membrane at distinct developmental stages. Right, maximum
163 intensity projections of GF with VPN colocalized pixels (orange) superimposed along GF
164 dendrites. Arrow and arrowheads indicate divergent dorsal and ventral VPN axons, respectively.
165 Scale bar, 20 μ m.

166 **(F,G)** Quantification of colocalization in (D,E) with colors corresponding to VPN type. Unpaired
167 Kruskal-Wallis test (LC4, $p = 2.088 \times 10^{-12}$; LPLC2, $p = 1.983 \times 10^{-10}$), Tukey-Kramer multiple
168 comparison test post hoc, * = $p < .05$ as compared to 36 hAPF, + = $p < .05$ as compared to 60
169 hAPF, # = $p < .05$ as compared to 72 hAPF. $N \geq 6$ hemibrains from ≥ 3 flies.

170 **(H,I)** 3D renderings of GF lateral dendrites (green) with LPLC2 (H, magenta) or LC4 (I, red)
171 colocalized pixels superimposed at distinct timepoints during development. Scale bar, 20 μ m. D -
172 dorsal, V - ventral, M - medial, L - lateral.

173 **(J)** Histograms of the spatial distribution of LC4 and LPLC2 contacts along the normalized
174 medial-lateral GF dendrite axis across development; colors are the same as in (H, I). N are as
175 stated in (F,G).

176

177 **Initial contacts between GF and VPNs are staggered in time**

178 We next investigated VPN axon targeting with respect to GF dendritic outgrowth. At
179 present, it is unknown when columnar VPN neurons are born³⁴, but these neurons may arise in
180 late larval to early pupal stages, a period when neuroblasts give rise to visual neurons (such as
181 T4/T5) that provide input to VPN dendrites in the lobula and lobula plate³⁵⁻³⁷. We hypothesized
182 VPNs would commence outgrowth and partner matching in coordination with GF dendrite
183 development. To visualize developmental interactions of select VPN and GF, we used existing¹¹
184 or newly developed VPN split-GAL4 driver lines screened for pupal expression (Supplemental
185 Figure 4), to concurrently label select VPN cell-types (*LC4_4-split-GAL4*, *LPLC2-split-GAL4*,
186 *LPLC1_1-split-GAL4*) and the GF (*GF_1-LexA*) over metamorphosis. To quantify interactions,
187 we employed our membrane colocalization method (Figure 1D) instead of synapse labeling
188 methods (such as t-GRASP³⁸) because we wanted to track all putative interactions, including
189 those that precede synapse formation, over time and did not want to create ectopic adhesions
190 between membranes. We additionally compared our membrane colocalization method to a

191 GRASP variant that is not restricted to presynaptic terminals²⁵ and found no statistical difference
192 between the number of colocalized or GFP positive pixels (Supplemental Figure 5).

193 Using colocalization as a proxy for membrane contacts, we investigated developmental
194 interactions between GF and its known adult partner VPNs, LC4 and LPLC2. We observed LC4
195 axonal extension and initial contact with GF at 24 hAPF (Figure 2F). At this timepoint, LC4
196 axons diverge into a dorsal fraction projected near the dorsal branch of the GF optic glomeruli
197 dendrites, and a ventral fraction projected towards the proximal regions of the GF dendrites
198 (Supplemental Figure 6). At 36 hAPF, contacts between the GF and LC4 increased, with both
199 dorsal and ventral fractions still apparent (Figure 2D, arrow, arrowhead, respectively). Although
200 *LPLC2-split-GAL4* shows obvious expression at this time, we did not observe any contacts
201 between LPLC2 and the GF (Figure 2E,G).

202 At 48 hAPF, LC4 and GF continued to show an increase in contacts (Figure 2F), and LC4
203 dorsal and ventral axons had converged (Supplemental Figure 6). At this time, approximately 24
204 hours after initial GF and LC4 contact, we observed GF contacts with LPLC2 (Figure 2E,G) as
205 the dorsal branch of the GF dendrites extended past LC4 axons (Supplemental Figure 6,
206 arrowhead). Altogether, our data suggest that during the first half of metamorphosis, as the GF is
207 seeking out synaptic partners, interactions with VPN are staggered in time.

208 After the initial establishment of contacts, we next observed a significant increase in
209 contacts between partner VPNs and GF from 60 hAPF to 72 hAPF (Figure 2D-G). At 84 hAPF
210 through eclosion, contacts between GF and both VPNs decreased and then stabilized. Our results
211 suggest that in the second half of metamorphosis, GF prioritizes dendritic outgrowth, enhances
212 contacts with partner VPN, and eventually refines and stabilizes contacts with appropriate VPN
213 partners, LC4 and LPLC2.

214 We next investigated interactions between GF and a neighboring VPN, LPLC1, that does
215 not maintain synapses with GF in adulthood (Supplemental Figure 2). We observed a relatively
216 small number of contacts between GF and neurons labeled with *LPLC1_1-split-GAL4*¹¹
217 appearing around 48 hAPF, peaking around 60 hAPF, and disappearing around 84 hAPF
218 (Supplemental Figure 7A,B). This driver line, however, may also label a subset of VPN that are
219 not LPLC1 during development (Supplemental Figure 7D,E), so we repeated our contact analysis
220 by generating two new LPLC1 driver lines, *LPLC1_2-split-GAL4* and *LPLC1_3-split-GAL4*
221 (Supplemental Figure 4). While these driver lines revealed GF and LPLC1 membranes are
222 adjacent at 60 hAPF, we observed minimal to no contacts with GF (Supplemental Figure 7C).
223 Altogether, these results suggest that early in development, GF contacts are already biased
224 towards VPNs that are synaptically coupled to the GF in the adult.

225

226 **LC4 and LPLC2 occupy and maintain distinct regions along the GF dendrite**

227 In the adult GF circuit, LC4 inputs are localized to the medial regions of GF dendrites,
228 whereas LPLC2 inputs are localized to the most lateral regions (Figure 1). It is unknown if this
229 medial-lateral segregation is established initially or arises over development. To address this, we
230 manually aligned the GF dendrites across brains and quantified the density of contacts along the
231 medial-lateral axis. Across all time points, we found minimal overlap between LC4 and LPLC2;
232 the peak density of contacts for LC4 and LPLC2 consistently occupied the most medial and
233 lateral regions, respectively (Figure 2H-J).

234 The GF optic glomeruli dendrites contain dorsal and ventral branches, therefore we
235 repeated the analysis of membrane contacts along the dorsal-ventral axis. At 48 hAPF, LPLC2
236 contacts were primarily confined to the dorsal regions, and LC4 to the ventral regions

237 (Supplemental Figure 8). This segregation was reduced at 60 hAPF and less obvious in the later
238 stages of development (84 hAPF – 96 hAPF), in alignment with previous investigations into
239 adult synapse localization along the dorsal-ventral axis⁷. Altogether, our results highlight the
240 importance of the medial-lateral division of LC4 and LPLC2 inputs onto GF dendrites, where
241 targeting is established early and maintained throughout development.

242

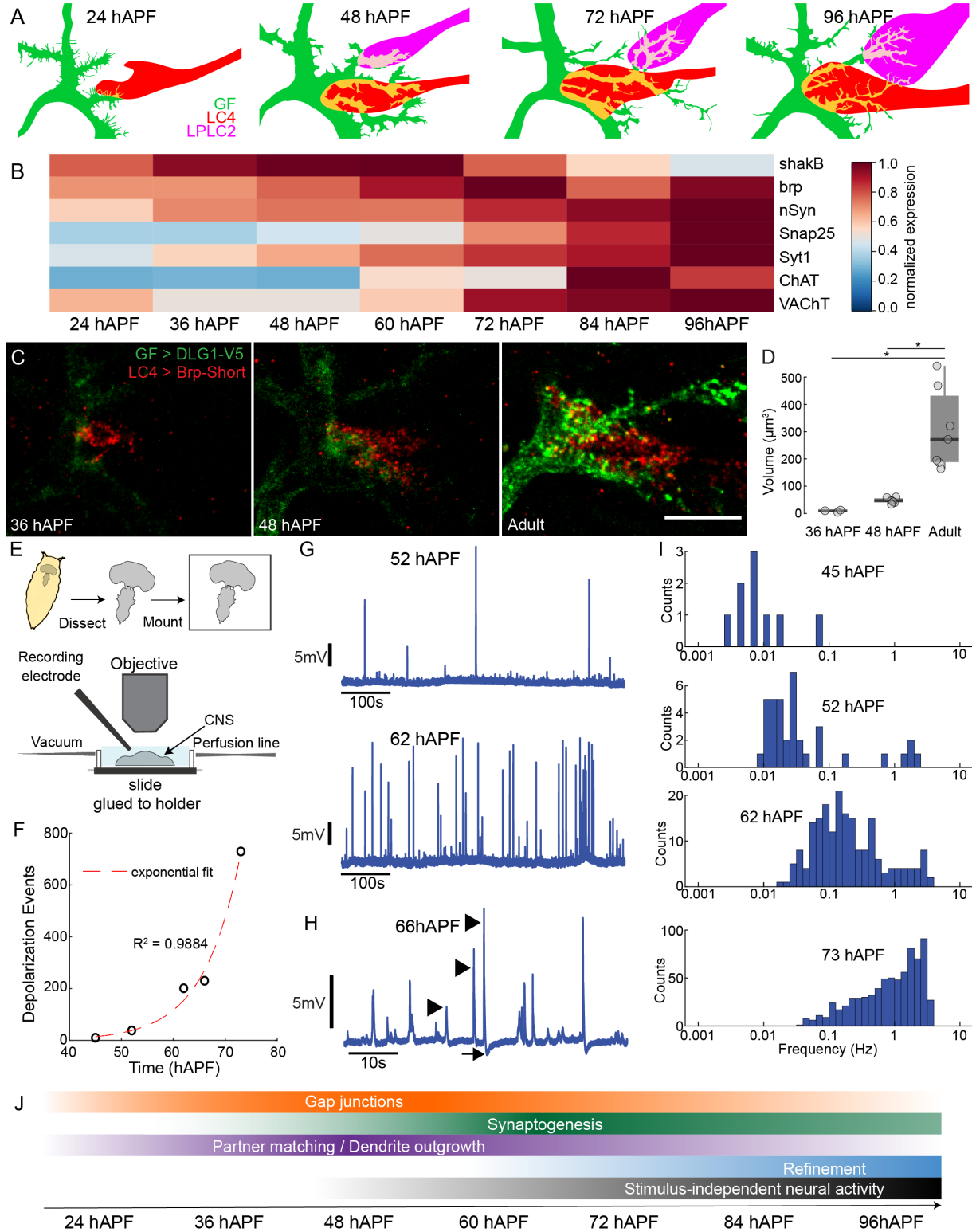
243 **Upregulation of synaptic machinery across key stages of metamorphosis**

244 Although our colocalization data provide the time course for interactions between VPN
245 axons and GF dendrites across development, they do not provide information on the timing of
246 synaptogenesis. We therefore investigated how our time course for GF/VPN interactions aligned
247 with the expression of presynaptic machinery (Figure 3A,B). We used a comprehensive scRNA-
248 seq atlas of the developing *Drosophila* visual system which profiled optic lobe neurons at
249 multiple time points across metamorphosis and identified both global and cell-type specific
250 transcriptional programs²².

251 As developmental clusters corresponding to LC4, LPLC2, and LPLC1 have been
252 identified in this dataset, we re-analyzed these data to determine when genes required for
253 synaptic transmission were upregulated in metamorphosis. We first investigated the expression
254 of *brp*, a presynaptic active zone protein that is homologous to the mammalian ELKS/CAST
255 family^{39,40} that is commonly used to label presynaptic terminals. We found *brp* to be present as
256 early as 24 hAPF and gradually increase up until 60 – 72 hAPF (Figure 3B, Supplemental
257 Figures 9,10). Presynaptic genes in the SNARE complex⁴¹⁻⁴⁴ *nSyb*, *cpx*, *Snap25* and *Syx1A* were
258 also present at early pupal stages, but significant upregulation was delayed with respect to *brp*,
259 from around 60 hAPF until the end of metamorphosis (Figure 3B, Supplemental Figures 9,10).

260 LC4, LPLC1 and LPLC2 are predicted to be cholinergic⁴⁴, and we found genes for cholinergic
261 synapse function (*ChAT* and *VACHT*) were upregulated in the late stages of metamorphosis (≥ 60
262 hAPF) (Figure 3A, Supplemental Figure 9-10), delayed from the initial appearance of
263 presynaptic machinery, but following the time course reported for other cholinergic neurons²².
264 This upregulation coincides with our observed decrease in GF dendritic complexity, and
265 refinement and stabilization of GF and VPN contacts (Figure 2F,G, Supplemental Figure 7A-C).
266 These data suggest that although a subset of presynaptic components are expressed and
267 potentially assembled early, VPN cholinergic machinery arrives too late to contribute to the
268 initial targeting and localization of VPN axons on GF dendrites. Cholinergic activity instead is
269 likely to participate in VPN and GF synapse refinement and stabilization.

270 Given the significant role electrical synapses play across development, we also examined
271 expression of the innexin family of gap junction proteins. Shaking-B (*shakB*) has been denoted
272 to be the predominant innexin over development²², and we also observed a significant increase as
273 early as 36 hAPF (Figure 3B, Supplemental Figures 9,10) with all other innexins showing
274 minimal to no expression across metamorphosis. *shakB* expression peaked between 48-60 hAPF,
275 followed by a significant decrease from 60 hAPF to 72 hAPF for all cell types (Supplemental
276 Figures 9,10). Interestingly, this decrease occurred as *ChAT* and *VACHT* increased, potentially
277 marking the transition from predominantly electrical synaptic coupling to chemical synaptic
278 coupling. A summary of our scRNA-seq analyses aligned to our developmental interaction
279 timecourse can be seen in Figure 3A,B.



280

281 **Figure 3. Synaptogenesis and the emergence of stimulus-independent neural activity**

282 (A) Schematic of GF and VPN developmental interactions

283 **(B)** Heatmap timecourse of average, normalized VPN mRNA expression of genes for electrical
284 and chemical synapse function. Data are from the optic lobe transcriptional atlas²² and individual
285 VPN expression patterns can be found in Supplemental Figure 9.
286 **(C)** Max intensity projections of a substack of DLG expression in GF (DLG1-V5, green) and Brp
287 puncta in LC4 (Brp-Short, red) at selected timepoints. Scale bar, 10 μ m.
288 **(D)** Quantification of volume of Brp colocalized with DLG from (C). Unpaired Kruskal-Wallis
289 test ($p = 0.001$), Dunn-Sidak comparison test post hoc, $* = p < .05$, $N = 3-7$ hemibrains from 2-5
290 flies.
291 **(E)** Schematic of *ex-plant* pupal electrophysiology preparation.
292 **(F)** The total number of identified depolarizing events increases exponentially (fit, dotted red
293 line) over time. $N = 5$ flies.
294 **(G)** Representative traces of GF membrane potential recordings using the pupal
295 electrophysiology preparation for two timepoints.
296 **(H)** Zoomed in recording showing features resolvable with electrophysiology. Arrow indicates
297 hyperpolarization following large depolarizing events, arrowheads indicate different event
298 amplitudes.
299 **(I)** Distribution of event frequencies from inter-event intervals.
300 **(J)** Timecourse of developmental stages as estimated from anatomical, scRNA-seq and
301 electrophysiology data.
302

303 **GF and VPN synapse assembly is initiated during the partner matching stages**

304 While our scRNA-seq data provide an estimate of gene expression across development,
305 relative levels of mRNA do not necessarily correlate linearly to protein translation⁴⁵. Therefore,
306 using our scRNA-seq data to guide our hypotheses, we next investigated the temporal expression
307 patterns of select pre- and postsynaptic proteins in VPN and GF. We utilized an iteration of
308 Synaptic Tagging with Recombination (STaR)⁴⁶ to visualize LPLC2 and LC4 specific Brp,
309 driven by its endogenous promoter and tagged with smGdP-V5. From our scRNA-seq data, *brp*
310 is expressed early in both LC4 and LPLC2 (Supplemental Figures 9,10). Using *LC4_4-split-*
311 *GAL4* and *LPLC2-split-GAL4* driver lines that turn on prior to 36 hAPF, we quantified the
312 fluorescence of V5-tagged Brp over metamorphosis (Supplemental Figure 11). We found Brp
313 already present in LC4 at 36 hAPF, as supported by the RNAseq data, and that Brp expression
314 increased until 60 hAPF. Unexpectedly, we witnessed a delay in the appearance and peak
315 expression of Brp in LPLC2, similar to the staggered arrival times of LC4 and LPLC2 onto GF

316 dendrites. It is possible that the assembly of synaptic machinery is delayed in LPLC2 to
317 accommodate its arrival time. However, because V5-tagged Brp expression is dependent not
318 only on the native *brp* promoter but also limited by when the VPN driver line turns on, the
319 differences in Brp appearance could also be due to temporal differences in the driver lines.
320 These data suggest presynaptic machinery is already present during initial partner matching
321 between VPN and GF and increases as contacts are refined and stabilized.

322 We next investigated whether Brp accumulating at presynaptic terminals in VPNs was
323 directly opposed to postsynaptic machinery, as an indicator of functional pre/postsynaptic sites.
324 To label presynaptic Brp in VPN, we established a new transgenic line that expresses Brp-Short
325 tagged with GFP under the control of the *lexAop* promoter (*lexAop-Brp-Short-GFP*). Brp-Short
326 is a truncated, non-functional Brp protein that localizes to sites of endogenous full-length Brp
327 without disrupting morphology or function⁴⁷ and has been used to map synaptic organization in
328 the *Drosophila* CNS^{48,49}. To label postsynaptic machinery in the GF, we targeted discs large 1
329 (*dlg1*), the fly PSD-95 ortholog⁵⁰ using *dlg1[4K]*, a conditional tagging strategy that enables
330 cell-type specific (*UAS-FLP*) V5-tagging of endogenous DLG1⁴⁹. Combining these tools with
331 our GF and VPN driver lines, we achieved co-expression of LC4-specific Brp-Short-GFP, and
332 GF-specific DLG1-V5 and investigated protein expression patterns at distinct developmental
333 stages. We observed faint, diffuse DLG1-V5 expression 36 hAPF (Figure 3C,D), around the time
334 when initial GF and VPN contacts are observed (Figure 2F). However, significant DLG1-V5 and
335 Brp-Short colocalization was not observed until 48 hAPF, although it remained only a small
336 fraction of what was witnessed in the adult (Figure 3C,D). Our data suggest that although pre-
337 and postsynaptic proteins are present at the initial stages of partner matching, it is not until
338 around 48 hAPF that they begin to assemble functional synaptic connections.

339

340 **GF exhibits stimulus-independent neural activity during development**

341 Our Brp-Short / DLG1-V5 dual labeling experiments suggest functional pre- and
342 postsynaptic sites are present around 48 hAPF. Interestingly, within fly optic lobe neurons,
343 sporadic and infrequent neural activity is first witnessed, through Ca²⁺ imaging, around 45
344 hAPF⁵¹. Developmental activity within DN_s has not been investigated, so we set out to
345 determine when activity first initializes within the GF and characterize GF activity patterns over
346 development. We developed an *ex-plant* pupal electrophysiology preparation for high resolution
347 recordings of the GF membrane potential over time (Figure 3E). Briefly, the entire pupal CNS
348 was dissected and mounted onto a coverslip, which was then attached to a customized holder that
349 enabled us to perfuse oxygenated extracellular saline during recordings. Using our preparation,
350 we recorded from the GF for approximately one hour in current-clamp mode at distinct
351 developmental time periods. At 45 hAPF, we witnessed sporadic, infrequent depolarizing events
352 (Figure 3F and Supplemental Figure 12), aligning with the emergence of activity in the optic
353 lobes⁵¹ and the initial opposition of Brp/DLG puncta (Figure 3C,D). The number of depolarizing
354 events increased exponentially as development progressed (Figure 3F,G, Supplemental Figure
355 12), mirroring the increased expression of cholinergic synaptic machinery within the scRNA-seq
356 data (Figure 3B, Supplemental Figures 9,10). As expected with an increase in the number of
357 depolarizing events, the interval between events decreased (inter-event frequency increased) as a
358 function of age (Figure 3I, Supplemental Figure 12).

359 Our recordings enabled us to observe hyperpolarizing events (Figure 3H, arrow) that
360 occasionally preceded large depolarizing events (Figure 3H, arrowheads), and small amplitude
361 events that would not be resolvable with Ca²⁺ imaging. We also observed a broad distribution in

362 event frequency (Figure 3G,I) instead of one dominant frequency from distinct alternating phases
363 between silence and activity as seen in optic lobe or whole brain Ca^{2+} imaging from 55 - 65
364 hAPF^{51,52}. It is possible our *ex-plant* preparation may alter activity patterns from those observed
365 *in-vivo*. Alternatively, our recordings report activity not resolvable in Ca^{2+} imaging, and central
366 brain neurons like the GF may display broader patterns as they pool input across many diverse
367 cell types. Altogether, our data (summarized in Figure 3J) suggest initial GF partner matching
368 precedes synaptogenesis. GF synapses become functional around 48 hAPF, with an upregulation
369 of gap junction proteins and the appearance of apposed pre and postsynaptic machinery
370 suggesting electrical (predominant) and chemical (minor) synapses contribute to the underlying
371 activity witnessed at this stage. In the later stages of development, the frequency of synaptic
372 events increase as gap junction proteins are downregulated and cholinergic presynaptic
373 machinery is upregulated to enhance and stabilize synapses with intended synaptic partners while
374 refining unintended contacts.

375

376 **LC4 ablation results in an increase of GF contacts with the LPLC2 glomerulus**

377 After establishing our timecourse of GF and VPN interactions, we next investigated
378 potential mechanisms that regulate VPN targeting and localization onto GF dendrites. Our data
379 suggest synaptic activity does not contribute to the initial stages of VPN to GF partner matching.
380 However, activity could be necessary for maintenance of the medial-lateral division of LC4 and
381 LPLC2 inputs on GF dendrites, as neuronal activity can be crucial for proper refinement⁵³⁻⁵⁷. To
382 test this, we attempted to silence LC4 during development by expressing the inwardly rectifying
383 potassium channel Kir2.^{17,58} using *LC4_4-split-GAL4*. However, we found early expression of
384 *Kir2.1* resulted in a significant loss of LC4 (Figure 4A; Supplemental Figure 13A-D). Expression

385 of *Kir2.1* with a driver line used in previous silencing experiments⁶ that turns on later in
386 development (*LC4_1-split-GAL4*) did not cause a loss of LC4 (Supplemental Figure 13A-D). As
387 our *LC4_4-split-GAL4* driver line turns on ~18 hAPF, prior to initial LC4 to GF contact, these
388 data suggest that overexpression of Kir2.1 early in development is detrimental to LC4 survival,
389 potentially due to the inability to compensate for disruptions in ionic homeostasis or the direct
390 induction of apoptosis⁵⁹⁻⁶¹. Co-expression of an apoptosis inhibitor p35⁶² with Kir2.1 using our
391 *LC4_4-split-GAL4* driver line, however did not prevent cell death (Supplemental Figure 13E,F),
392 potentially due to redundancies in apoptosis pathways or the relative timing of expression.

393 With our finding we could use Kir2.1 as a tool to ablate LC4, we reframed our question
394 to examine how the physical loss of LC4 alters LPLC2 morphology and targeting. Given that
395 LC4 contacts GF dendrites ~24 hours prior to LPLC2, we wondered if LC4 physically restricts
396 LPLC2 from extending to medial regions of the GF optic glomeruli dendrites. We expressed
397 tdTomato in LPLC2 using a LexA driver line (*LPLC2-LexA*) while simultaneously driving
398 myrGFP or Kir2.1 with *LC4_4-split-GAL4*. In adult flies where Kir2.1 expression ablated the
399 majority of LC4, the LPLC2 axon bundle extended into areas where the LC4 glomerulus would
400 be expected and we witnessed a significant increase the LPLC2 glomerulus volume (Figure
401 4B,C). Due to the witnessed expansion of the LPLC2 glomerulus, we next investigated whether
402 the loss of LC4 increased the territory GF dendrites occupied within the LPLC2 glomerulus. We
403 expressed Kir2.1 with *LC4_4-split-GAL4* to achieve LC4 cell death, while simultaneously
404 expressing tdTomato in GF using *GF_1-LexA*. We identified the LPLC2 glomerulus using a
405 neuropil label (Brp) and again found that LC4 cell loss resulted in an LPLC2 glomerulus with
406 altered morphology as compared to control flies (Figure 4D,E). We then quantified the overlap
407 between GF dendrites and the LPLC2 glomerulus (Figure 4F). We found that LC4 ablation more

408 than doubled the amount of colocalization between GF dendrites and the LPLC2 glomerulus,
409 with the glomerulus expanding onto more medial regions of the GF dendrites as compared to
410 controls (Figure 4D-F). In summary, our data demonstrate LC4 ablation results in altered LPLC2
411 axonal morphology and increased GF dendritic arborizations within the LPLC2 glomerulus,
412 suggesting the early arrival and physical presence of LC4 may impede LPLC2 from contacting
413 more medial regions of the GF.

414 To revisit our original question as to whether activity influences GF and VPN
415 connectivity, we expressed Kir2.1 in LC4 using our late, *LC4_1-split-GAL4* driver line, and
416 tdTomato in GF using our *GF_1-LexA* driver. The *LC4_1-split-GAL4* driver line should be
417 effective at silencing LC4 as it expresses Kir2.1 prior to the onset of GF activity, as witnessed
418 here (Figure 3F,G , Supplemental Figure 12), and Ca²⁺ activity, as observed in the fly's visual
419 system⁵¹. We found no significant difference in the density or localization of contacts between
420 GF and LC4 whether we expressed Kir2.1 or myrGFP in LC4 (Figure 4G,H). These data suggest
421 LC4 localization along GF dendrites is activity independent, and the early arrival and physical
422 presence of LC4 axons restricts LPLC2 targeting to the lateral regions of GF dendrites.

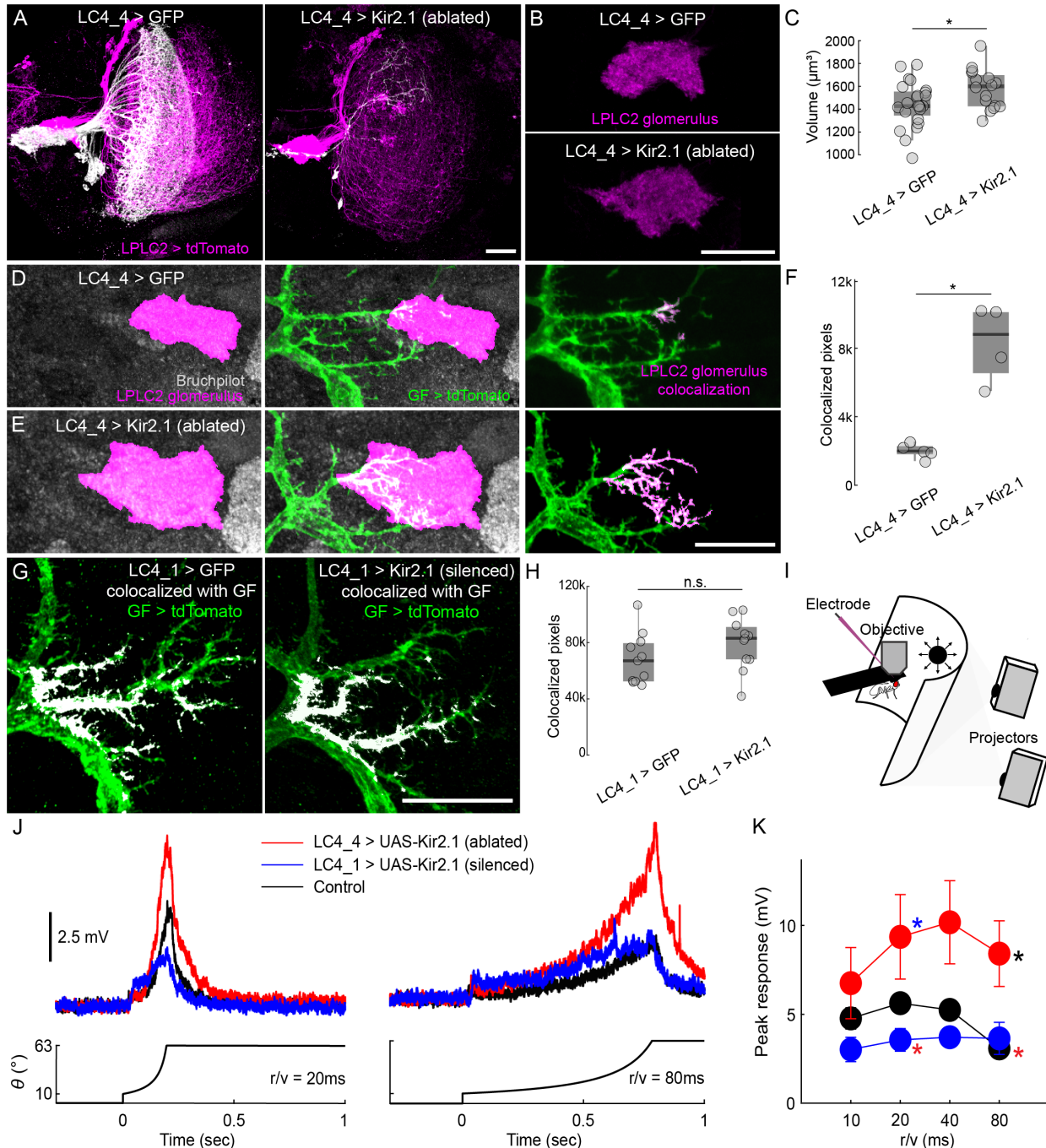
423

424 **Functional compensation in the GF circuit occurs after LC4 ablation**

425 Our anatomical data suggest the loss of LC4, but not silencing of its activity, during
426 development results in a reconfiguration of contacts between LPLC2 and GF. We next
427 investigated whether the apparent change in connectivity had functional consequences, affecting
428 GF's encoding of ethologically relevant visual stimuli. GF are tuned to looming stimuli – the 2D
429 projections of an object approaching on a direct collision course. LC4 provides to the GF
430 information about the angular speed while LPLC2 provides information about the angular size of

431 a looming object^{6,7}. We recorded GF responses in tethered, behaving flies using whole-cell patch
432 clamp electrophysiology⁶³ (Figure 4I). We displayed looming stimuli across different radius to
433 speed (r/v) ratios where the contributions of LC4 and LPLC2 to the GF response have been
434 previously established^{6,7}. In control animals, LPLC2 contributions are maintained across stimuli,
435 as the range in stimulus size does not change, while LC4 contributions increase as stimuli
436 become more abrupt⁶.

437 We found, as reported previously⁶, that silencing LC4 by expressing Kir2.1 using the
438 *LC4_1-split-GAL4* driver line reduced the GF response to looming stimuli as stimuli became
439 more abrupt (Figure 4I-K). To further verify Kir2.1 silencing was effective, we expressed Kir2.1
440 in lamina monopolar cells 1 and 2 (L1-L2), the early-stage inputs to motion vision processing^{64,65}
441 which ameliorated GF responses, as reported previously⁶ (Supplemental Figure 14). However,
442 in contrast to what we witnessed with silencing, we found the ablation of the majority of the LC4
443 population, by expressing Kir2.1 with our *LC4_4-split-GAL4* driver line, resulted in an enhanced
444 GF response to looming stimuli (Figure 4I-K), aligned with the observed increase in GF
445 dendrites occupying the LPLC2 glomerulus (Figure 4D-F). Our data support that the
446 developmental reorganization of LPLC2 and GF following LC4 ablation is functionally
447 significant and leads to an over-compensation in the GF looming response.



448

449

Figure 4. Developmental ablation of LC4 with Kir2.1 alters the morphology of the LPLC2 glomerulus and increases LPLC2 contacts and functional drive onto GF.

450 (A) Maximum intensity projections of LPLC2 expressing tdTomato (magenta) and LC4 (white) expressing GFP (left) or Kir2.1 (right) using LC4_4, a driver line that turns on early in development. Scale bar, 20 μm .

451 (B) Maximum intensity projections of a substack of the LPLC2 glomerulus (magenta) in a fly where LC4 express GFP (top) or are ablated through Kir2.1 expression (bottom). Scale bar, 20 μm .

456

457 (C) Quantification of LPLC2 glomerulus volume in (B). Two-sample *t*-test, $p = .0273$, $N = 16-24$
458 hemibrains from 8-13 flies.

459 (D) Maximum intensity projections of Brp (NC82, gray) with the LPLC2 glomerulus highlighted
460 (magenta) in a fly where GFP was expressed early in LC4 (left). Maximum intensity projections
461 of GF dendrites (tdTomato, green) extending into the LPLC2 glomerulus (middle). Maximum
462 intensity projections of colocalized pixels (magenta) between GF and the LPLC2 glomerulus
463 superimposed onto the GF (right).

464 (E) Maximum intensity projections of Brp (gray) with the LPLC2 glomerulus highlighted
465 (magenta) in a fly where Kir2.1 was expressed early to ablate LC4 (left). Maximum intensity
466 projections of GF dendrites (tdTomato, green) extending into the LPLC2 glomerulus (middle).
467 Maximum intensity projections of colocalized pixels (magenta) between GF and the LPLC2
468 glomerulus superimposed onto the GF (right). Scale bar, 20 μ m.

469 (F) Quantification of colocalization between GF and the LPLC2 glomerulus from (D,E).
470 Unpaired Mann-Whitney U test, $p = .0159$, $N \geq 4$ hemibrains from ≥ 4 flies.

471 (G) Maximum intensity projections of GF expressing smGFP (green) with colocalized pixels
472 (white) between LC4 expressing GFP (left) or silenced by Kir2.1 (right) using an LC4-split-Gal4
473 driver that turns on late during development (*LC4_1-split-GAL4*). Scale bar, 20 μ m.

474 (H) Quantification of colocalization in (G). Unpaired Mann-Whitney U test, $p = .1486$, $N \geq 11$
475 hemibrains from ≥ 6 flies.

476 (I) Schematic representing *in-vivo* electrophysiology setup for head-fixed adult flies. Visual
477 stimuli (looms) were presented ipsilateral to the side of the recording via projection onto a screen
478 positioned in front of the fly.

479 (J) Average GF responses to select looming stimuli presentations of different radius to speed
480 ratios (r/v).

481 (K) Quantification of peak amplitude responses to looming stimuli presentations in (J). Unpaired
482 Kruskal-Wallis test ($r/v = 10\text{ms}$, $p = .1105$; $r/v = 20\text{ms}$, $p = .0443$; $r/v = 40\text{ms}$, $p = .0556$; $r/v =$
483 80ms , $p = .0385$), Tukey-Kramer multiple comparison test post hoc, $* = p < .05$, $N = 6-8$ flies.

484

485

486 DISCUSSION

487 Here, our investigation into the interactions of GF dendrites and VPN axons support a
488 developmental program where GF and partner VPNs make initial contact in precise, stereotyped
489 regions that are maintained into eclosion through competitive, physical interactions. Ablation of
490 one major VPN partner (LC4) results in territory expansion of another VPN (LPLC2) that
491 confers compensatory functional changes within the GF circuit. After initial VPN territories are
492 established, GF dendrites continue to arborize and increase contacts with VPNs, while avoiding
493 contacts with non-synaptic neighbors. This developmental stage coincides with an upregulation
494 of gap junctions, the opposition of pre- and postsynaptic proteins, and the onset of developmental

495 activity in the GF. This outgrowth is followed by a period of stabilization/refinement that
496 coincides with an upregulation of cholinergic synaptic machinery and an increase in the
497 frequency of developmental activity in the GF. This developmental time course is summarized in
498 Figure 3A,J. Our data establish the GF escape circuit as a sophisticated developmental model
499 that can be used to study mechanisms establishing integration of sensory inputs within a
500 sensorimotor circuit, the role neural activity plays in shaping circuit connectivity and refinement,
501 and the relationship between expressed genes and circuit development and function.

502 The development of the *Drosophila* visual system proceeds in a series of steps which
503 likely serve to reduce the complexity of wiring paradigms from neurons of the same or
504 neighboring cell-types, highlighting the importance of timing⁶⁶. We found staggered interactions
505 of the GF with VPN partners, where LC4 contacts the GF approximately 24-36 hours prior to
506 LPLC2. This staggered arrival of VPN axons could reduce the complexity of decisions made by
507 the GF during partner matching, as is also seen in the olfactory glomeruli in an *ex-plant*
508 preparation where axons of pioneer olfactory receptor neurons (ORNs) terminate in posterior
509 regions, and ORNs arriving later terminate in anterior regions⁶⁷. From 36-72 hAPF, we observe
510 an increase in GF dendritic complexity and extension and increase in contacts with VPN
511 partners, coordinated with an upregulation of genes involved in the SNARE complex (Figure
512 3A,B). This period of precise targeting and outgrowth likely reflects a robust partner matching
513 program, potentially through ligand-receptor or attractive/repulsive cues⁶⁸. Our confocal data
514 provide high-resolution snapshots of membranes at distinct periods over metamorphosis, but as
515 metamorphosis is a dynamic process, future work could incorporate time-lapsed imaging to
516 investigate transient interactions that may have been missed.

517 Our GF and VPN colocalization data show a developmental progression that begins with
518 partner matching between VPN and GF in stereotyped regions, an increase of contacts with
519 synaptic partners, proceeded by refinement as neurons assume their adult morphology.
520 Comparison with the time course of scRNA-seq data provides insight into genes that may play a
521 role in these processes. We find gap junction coupling may serve a role in partner matching, as
522 *shakB* expression is high at this time (Supplemental Figure 9)²². Our data also support a
523 transition from predominantly electrical to chemical synapses as witnessed in other species^{69,70} at
524 the onset of refinement. *shakB* is downregulated while cholinergic synaptic machinery *ChAT* and
525 *VAcHT* (Figure 3B and Supplemental Figures 9,10) are upregulated. Our model system is well
526 poised to investigate the role of electrical and chemical signaling, and their supporting genes, in
527 circuit development and function.

528 We provide the first electrophysiological recordings of developmental neural activity in
529 pupal neurons, a phenomenon that has been documented in developing vertebrate systems, and
530 recently proposed within the fly with Ca²⁺ imaging^{53-57,69,71-75}. Our data demonstrate activity in
531 the GF emerges as early as 45 hAPF, and increases in frequency as a function of time. While
532 scRNA-seq data and our Brp-Short and DLG1-V5 protein expression data suggests this activity
533 is driven through functional electrical and chemical synapses, changes in GF intrinsic properties
534 may also contribute to witnessed changes in frequency. For example, recordings from the
535 superior olivary nucleus in the avian auditory brainstem over embryonic development to
536 hatching show neuronal excitability increases due to changes in K⁺ and Na⁺ ion channel
537 conductance⁷⁶, therefore further investigation into what drives these changes in GF activity is
538 warranted.

539 To record spontaneous activity in pupal GF neurons we developed an *ex-plant* system
540 that differs from established *ex-vivo* systems⁷⁷⁻⁷⁹ in that we are not attempting to culture our ex-
541 plant long term and replicate *in-vivo* conditions through the addition of ecdysone to aid neuronal
542 development. To our knowledge, developmental activity within these ex-vivo systems has yet to
543 be reported. We find in our ex-plant noticeable similarities to the recent discovery of *in-vivo*
544 activity patterns in the developing fly nervous system⁵¹. We first observe GF stimulus
545 independent activity (stimulus independent because all sensory organs are no longer connected)
546 as infrequent events around 45 hAPF, similar to sparse Ca²⁺ activity witnessed in the fly optic
547 lobes at this same time⁵¹. As development progresses, the frequency of depolarizing events in
548 the GF increases, similar to what has been reported *in-vivo*. However, we find no discernible
549 phases of activity and silence as observed *in-vivo* via calcium imaging around 55-65 hAPF,
550 classified as the periodic stage of patterned, stimulus independent neural activity (PSINA). We
551 instead witness a progression into what resembles the later turbulent phase of PSINA that occurs
552 around 70 hAPF to eclosion⁵¹. As *in-vivo* activity in individual developing DNs or central brain
553 neurons has as of yet to be reported, our data could represent actual *in-vivo* activity patterns from
554 neurons in the central brain where multiple inputs converge. Alternatively, even if our removal
555 of the CNS disrupts activity patterns observed *in-vivo*, our ex-plant could provide a highly
556 accessible model system to uncover the underlying mechanisms for how particular activity
557 patterns arise.

558 The location of a synapse on a dendrite can impact its overall effect on a neuron, and
559 establish how it contributes to neural computations⁸⁰⁻⁸². We find the location of synapses of each
560 VPN cell type to be highly stereotyped, suggesting location may impact computation, although
561 this has yet to be directly investigated. Our contact data suggest that targeting of LC4 and

562 LPLC2 to their respective regions is established upon initial contact instead of refinement in the
563 later stages of development. This is noticeably different from ORN axonal targeting to olfactory
564 glomeruli, where axons target many neighboring glomeruli and are eventually refined to a
565 specific glomerulus^{67,83,84}. It is possible specific protein interactions establish LC4 and LPLC2
566 target specificity^{68,85-87}, similar to how basket interneurons target the axon initial segment of
567 Purkinje cells in the vertebrate cerebellum via localized cell adhesion molecules and adaptor
568 proteins⁸⁸⁻⁹¹. Our data, however, support that axon arrival times also play a role, with LC4 first
569 contacting GF dendrites in medial regions, physically impeding LPLC2, and leaving LPLC2
570 segregated to the lateral regions. This physical barrier may explain why LPLC2 is able to extend
571 into medial regions following LC4 ablation (Figure 4D-F). We do however find LPLC2 does not
572 fully replace LC4 along the dendrites, suggesting segregation may arise from a combination of
573 physical restraints from LC4 and potentially other neurons, in addition to molecular interactions.
574 It does not appear that activity-based mechanisms influence the localization of LC4 and LPLC2
575 to specific regions because silencing activity in LC4 does not result in significant changes in
576 LC4/GF contact density or localization (Figure 4G,H). In addition, elimination of the majority of
577 LC4 neurons did not affect targeting of the remaining LC4 neurons to the GF dendrites in the
578 expected regions.

579 We also report altered GF output to looming stimulus presentations (Figure 4J,K)
580 following LC4 ablation as an example of developmental plasticity to preserve an evolutionary
581 conserved escape behavior that is critical to the fly's survival. Because we observe a significant
582 increase in GF dendritic occupancy within the LPLC2 glomerulus, our prevailing hypothesis is
583 that LPLC2 synaptic inputs to GF have increased. Alternatively, the 1-7 LC4 neurons that remain
584 after ablation may also have increased synaptic input, however the consistency of the

585 compensatory responses as looming stimulus parameters change (r/v) and the limited visual field
586 coverage with just 1-7 LC4 neurons supports compensation through remaining LC4 is unlikely to
587 underlie the enhanced GF responses.

588 While we here demonstrate stereotyped targeting of VPNs to distinct regions on GF
589 dendrites, emerging work suggests an additional level of targeting may occur within individual
590 VPNs. It was previously suggested, based on light microscopy data, that retinotopy is lost within
591 the seemingly random terminations of VPN axons in most optic glomeruli, unlike in vertebrate
592 systems where established retinotopy in the retina is maintained in projections to the lateral
593 geniculate nucleus and superior colliculus/tectum⁹²⁻⁹⁴. However, recent evidence suggests VPNs
594 preserve spatial information by biasing synaptic input to postsynaptic neurons relative to their
595 receptive field^{8,10,19}. This is seen in LC4 synaptic inputs to postsynaptic DNp02 and DNp11
596 neurons, where LC4 synaptic inputs to DNp02 increase along the posterior to anterior visual
597 axis, and LC4 synaptic inputs to DNp11 increase along the anterior to posterior visual axis¹⁰.
598 LC4 inputs to GF do not appear to bias synapse numbers based on their receptive field, but a bias
599 of synaptic inputs from LPLC2 to GF exists along the ventral to dorsal axis¹⁰. As synaptic
600 gradients appear to be utilized amongst many VPN neurons, our model system is well poised to
601 investigate when and how these synaptic biases arise.

602 In summary, our data provides a detailed anatomical, transcriptomic, and functional
603 description of GF and VPN development. Our model is unique in that we can observe multiple
604 visual feature inputs competing for dendritic space, providing a complex sensorimotor model to
605 the field that will be useful to determine the relationship between connectivity and sensorimotor
606 integration. The GF also receives input from other brain regions outside of the optic glomeruli⁹⁵,
607 and it would be interesting to characterize the development of GF with respect to these other

608 regions and further investigate how these inputs influence GF output. Finally, these VPN are
609 only a few of the 20+ VPN that terminate in the optic glomeruli, and GF is one of hundreds of
610 DNs, expanding the opportunity to uncover conserved, fundamental mechanisms for the wiring
611 of sensorimotor circuits.

612

613 **METHODS**

614 **Fly genotypes and rearing**

615 *Drosophila* stocks (Table 1) and experimental crosses (Supplementary Table 1) were
616 reared on a traditional molasses, cornmeal, and yeast diet (Archon Scientific), maintained at
617 25°C and 60% humidity on a 12-hour light/dark cycle, except for optogenetics experiments
618 where dark reared flies were raised on 0.2 mM retinal food as larva and switched to 0.4 mM
619 retinal food following eclosion. All experiments were performed on pupal or adult female flies 2-
620 5 days post-eclosion. New split-GAL4 drivers lines SS02569 and SS02570 were generated using
621 previously described methods¹¹. The Janelia FlyLight Project Team contributed to split-GAL4
622 screening and stock construction.

623

624 Table 1. *Drosophila* Stocks

DROSPHILA STOCKS	SOURCE	IDENTIFIER
<i>UAS-myr::smGFP-HA, lexAop-myr::smGFP-V5 (smGFP): pJFRC200-10XUAS-IVS-myr::smGFP-HA (attP18), pJFRC216-13XlexAop2-IVS-myr::smGFP-V5 su(Hw)attP8;;.</i>	Nern et al., 2015 ⁹⁶	

UAS-Kir 2.1_1: <i>w+; pJFC49-10xUAS-IVS-eGFP Kir2.1 (Su(Hw)attP6);</i>	Michael Reiser, Ed Rogers, Janelia Research Campus	
UAS-Kir 2.1_2: <i>w+;; pJFRC49-10xUAS-IVS-eGFP-Kir2.1 (attP2)</i>	Pfeiffer et al., 2012 ⁵⁸ ; von Reyn et al., 2014 ¹⁷	
smGdP-STaR: ; <i>LexAop-myr::tdTomato, UAS-R; brp-RSR-SmGdP-V5-2A-LexA</i>	Peng et al., 2018 ⁴⁶	
UAS-myr:GFP: <i>pJFRC12-10XUAS-IVS-myr::GFP (su(Hw)attP1);;</i>	Pfeiffer et al., 2012 ⁵⁸	
UAS-tdTomato: <i>pJFRC22-10xUAS-IVS-myr::tdtomato (su(Hw)attP8);;</i>	Pfeiffer et al., 2012 ⁵⁸	
GF_2-LexA, lexAop-GFP; UAS-Kir: <i>w+; 68A06-LexAp65 (VK00022), pJFRC57-13XLexAop2-IVS-GFP-p10 (su(Hw)attP5)/(CyO); pJFRC49-10XUAS-IVS-eGFPKir2.1 (attP2)/(TM6b)</i>	Ache et al., 2019 ⁷	
UAS-p35: <i>3rd chromosome</i>	Pecot et al., 2014 ⁶²	
GRASP: ; <i>lexAop-GFP_11; UAS-GFP_1-10</i>	Gordon & Scott, 2009 ²⁵	
UAS-CsChrimson: <i>UAS-CsChrimson-mVenus (attp18);;</i>	Klapoetke et al., 2014 ⁹⁷	
GF_1-LexA (early GF): <i>;; VT042336_LexA (attP2)</i>	Tirian & Dickson, 2017 ²⁴	
GF_2-LexA (late GF): <i>;68A06 LexA (VK00022);</i>	Pfeiffer et al., 2010 ⁹⁸	
GF_1-GAL4: <i>;; VT042336_GAL4 (attP2)</i>	Tirian & Dickson, 2017 ²⁴	

LC4_4-split-GAL4 (early LC4): ;R49C04_P65ADZp (attP2); R86D05_ZpGbd (attP40)	This study	
LC4_1-split-GAL4 (SS00315) (late LC4): ;R47H03_P65ADZp (attP40); R72E01_ZpGbd (attP2)	Wu et al., 2016 ¹¹	
LPLC1_1-split-GAL4 (OL0029B): ;R64G09_P65ADZp (attP40);R37H05_ZpGbd (attP2)	Wu et al., 2016 ¹¹	
LPLC1_2-split-GAL4 (SS02569): R64G09_P65ADZp (attP40); VT045990_ZpGbd (attP2)	This study	
LPLC1_3-split-GAL4 (SS02570): R64G09_P65ADZp (attP40); VT063739_ZpGbd (attP2)	This study	
LPLC2-split-GAL4 (OL0048B): ;R19G02_P65ADZp (attP40);R75G12_ZpGbd (attP2)	Wu et al., 2016 ⁹⁹	
LPLC2_LexA: ;75G12-LexAp65 (attP40);	Pfeiffer et al., 2010 ⁹⁸	
LC4-LexA: ;93G05-LexA (attP40);	Pfeiffer et al., 2010 ⁹⁸	
LC11-split-GAL4 (OL0015B): ;22H02_p65ADZp (attP40); R20G06_ZpGbd (attP2)	Wu et al., 2016	
L1/L2-split-GAL4 (SS00797): w+; R48A08-p65ADZp in attP40; R29G11-ZpGbd in attP2)	Tuthill et al., 2013 ⁶⁵	
dlg1[4K]	Parisi et al., 2023 ⁴⁹	
UAS-TNT: UAS-TeTxLC.tnt	Sweeney et al., 1995 ¹⁰⁰	
lexAop-Brp-Short-GFP	This study	

626 **Developmental staging**

627 Pupal staging across developmental time points has been previously described⁹⁹. In brief,
628 the sex of white pre-pupa was identified, and females were transferred to a separate petri dish,
629 marked as 0 hours after pupa formation (hAPF), and reared for the appropriate amount of time at
630 25°C before dissection. Dissections were performed within a 2-hour window of a targeted pupal
631 developmental stage. All pupal dissections were synchronized and processed through
632 immunohistochemistry protocols for pixel intensity measurements of images.

633

634 **Immunohistochemistry**

635 All dissections were performed in cold Schneider's insect media (S2, Sigma Aldrich,
636 #S01416) within a 15-minute window before solution exchange to avoid tissue degradation.
637 Brains were then transferred to a 1% paraformaldehyde (20% PFA, Electron Microscopy
638 Sciences, #15713) in S2 solution and fixed overnight at 4°C while rotating.
639 Immunohistochemistry was performed as described previously⁹⁶. Primary and secondary
640 antibodies are listed in Table 2. Supplementary Table 1 lists antibodies used for each figure with
641 their respective dilutions. Following immunostaining, brains mounted onto poly-L-lysine (Sigma
642 Aldrich, #25988-63-0) coated coverslips were dehydrated in increasing alcohol concentrations
643 (30, 50, 75, 95, 100, 100) for 5 minutes in each, followed by two 5-minute Xylene clearing steps
644 (Fisher Scientific, #X5-500). Coverslips were mounted onto a prepared slide (75 x 25 x 1 mm)
645 (Corning, #2948-75X25) with coverslip spacers (25 x 25 mm) (Corning, #2845-25) placed on
646 each end of the slide to prevent brain compression. Brain mounted slides were left to dry for at
647 least 48 hours prior to imaging.

648

649 Table 2. Resources and Reagents

RESOURCES OR REAGENTS	SOURCE	IDENTIFIER
Mouse anti-nc82	DSHB	CAT# - AB2314866 RRID: AB_2314866
Rabbit anti-GFP	Life technologies	CAT# - A11122 RRID: AB_221569
Chicken anti-GFP	EMD Millipore	CAT# - AB16901 RRID: AB_11212200
Rabbit anti-HA	Cell Signaling Technologies	CAT# - C29F4 RRID: AB_1549585
Alexa Fluor 488 goat anti-chicken	Invitrogen	CAT# - A11039 RRID: AB_2534096
Alexa Fluor 488 goat anti-rabbit	Invitrogen	CAT# - A11034 RRID: AB_2576217
Alexa Fluor 568 goat anti-rabbit	Invitrogen	CAT# - A11011 RRID: AB_143157
Alexa Fluor 568 goat anti-rat	Life technologies	CAT# - A11077 RRID: AB_2534121
Alexa Fluor 647 goat anti-Mouse	Life technologies	CAT# - A21236 RRID: AB_2525805
DyLight 550 anti-HA	Invitrogen	CAT# - 26183-D550 RRID: AB_2533052

DyLight 488 anti-HA	Invitrogen	CAT# - 26183-D488 RRID: AB_2533051
DyLight 550 anti-V5	Bio-rad	CAT# - Mca1360D550GA RRID: AB_2687576
DyLight 650 anti-V5	Invitrogen	CAT# - MA5-15253- D650 RRID: AB_2527642
Living Colors DsRed Polyclonal Antibody	TakaraBio	CAT# - 632496 RRID: AB_10013483
Mouse anti-Broad	DSHB	CAT# - AB_528104 RRID: AB_528104
KDo2 lexAop2rev_PspXI: 5' TGACcctcgagCGTTCAGCTGCGCTTGTTTATT 3'	This study	
KDo1 lexAop2for: 5' TCCGCGTTTCCAGACTTTAC 3'	This study	

650

651 **Confocal Microscopy**

652 Unless otherwise stated, all images were taken on an Olympus Fluoview 1000 confocal
653 system. Images were taken with a 60x, 1.42 NA oil immersion objective to achieve a voxel size
654 of .103 μ m x .103 μ m x .45 μ m. Imaging parameters were minimally adjusted between images to
655 achieve an image that utilizes the full pixel intensity range without oversaturating pixels. This

656 was necessary as driver lines in earlier pupal developmental periods showed lower levels of
657 expression than in later pupal developmental stages, therefore imaging parameters were adjusted
658 to optimize the membrane signal-to-noise ratio for each developmental stage that would allow
659 for optimized mask generation used in image analysis. In analyses where pixel intensities were
660 compared across developmental stages, all imaging parameters were kept consistent across all
661 images. STaR images were taken on a Zeiss LSM 700 with a 63x, 1.4 NA oil immersion
662 objective to achieve a voxel size of $.06\mu\text{m} \times .06\mu\text{m} \times .44\mu\text{m}$. Imaging parameters were kept
663 consistent to allow for comparison across all samples. Images for LPLC2 glomerulus volume
664 quantification were taken on a Zeiss LSM 700 with a 63x, 1.4 NA oil immersion objective with a
665 magnification of 0.50 to achieve a voxel size of $.0992\mu\text{m} \times .0992\mu\text{m} \times .3946\mu\text{m}$.

666

667 **Electron Microscopy**

668 The publicly available electron microscopy hemibrain dataset (version 1.2.1)²¹ was used
669 in this paper. NeuPrint²³ was used to create renderings and connectivity diagrams.

670

671 **Image analyses**

672 A region of interest (ROI) was drawn around the GF optic glomeruli dendrites to quantify
673 dendritic complexity and length. To quantify dendritic complexity, all pixels in this ROI were
674 summed. The Euclidean distance was measured from the beginning (most medial aspect) of the
675 GF optic glomeruli dendrites to the tip to calculate dendritic length.

676 To quantify membrane colocalization between GF and VPN neurons across development,
677 intensity-based thresholding was first used to generate a binary mask of each neuron membrane.
678 Using a custom GUI written in MATLAB, threshold values were manually selected to include

679 processes of each cell-type while excluding background and regions of the neuron that were out
680 of focus in each z-plane. Generated binary masks were inspected to make sure each mask was
681 representative of the imaged neuron membrane channel. In certain cases, the set threshold did not
682 include very fine neurites that were difficult to discriminate from background. Lowering
683 threshold values to capture these processes in the mask would result in background being
684 included into the mask as well, therefore generated masks may exclude some of the finer
685 dendritic processes with low SNR. Using these masks, colocalized pixels were collected plane-
686 by-plane across the entire image stack using Boolean operators between GF and VPN masks.
687 This output matrix resulted in a z-stack where only GF and VPN membranes were colocalized.
688 In some images, GF membrane labeling had a low SNR and prevented accurate mask generation
689 and was therefore excluded from analyses. In some cases, non-GF and non-VPN cell-types were
690 labeled with the driver lines, therefore these data were excluded from analyses. To increase rigor,
691 a second method to quantify GF to VPN membrane colocalization was used. Confocal stacks of
692 labeled neuronal membranes were 3D rendered in Imaris using the Surfaces function. Thresholds
693 were manually applied to generate 3D masks of neuronal membranes so that the rendered 3D
694 image was representative of the imaged membrane. Similar to MATLAB thresholding, in certain
695 cases the set threshold did not include fine neurites as they were difficult to discriminate from the
696 background using automated algorithms. Following initial 3D membrane renderings, renderings
697 were inspected and regions where faint processes were still visible but not detected in the
698 thresholding pipeline were manually filled in using the ‘Magic Wand’ function. Once 3D
699 rendering was complete, areas of colocalization were identified using the ‘Surface-Surface
700 contact area’ XTension, and the volume of this output was quantified.

701 To determine the density of VPN contacts along the GF optic glomeruli dendrite, a z-
702 projection of the GF was manually aligned and rotated using anatomical landmarks consistently
703 observed to align the lateral dendrite along the medial-lateral axis (x-axis). The same rotation
704 and alignment were applied to the appropriate membrane colocalization matrix. An ROI was
705 then drawn around the GF optic glomeruli dendrites, with anatomical landmarks consistently
706 observed used to denote the beginning and end of the optic glomeruli dendrite. To account for
707 variation in the optic glomeruli dendrite extension across images, we normalized the x-axis to the
708 length of the drawn ROI (i.e., GF lateral dendrite). To determine where VPN contacts were
709 localized along the dorsal-ventral axis (y-axis), the same images were used, but normalized the
710 y-axis to the length of the drawn ROI. Total colocalized pixels were summed along each column
711 or row, respectively, and the pixel density for each column or row was averaged across brains in
712 each condition, then plotted along the normalized axis.

713 To quantify the average pixel intensity of VPN-specific Bruchpilot (Brp) puncta across
714 developmental timepoints, VPN masks were generated from the membrane channel using the
715 same pipeline used for the GF and VPN membrane colocalization. These binary masks were then
716 multiplied to the Brp-puncta channel to gather raw pixel intensities for Brp-V5 puncta localized
717 to the VPN membrane. The total intensity sum of the glomerulus was divided by the total
718 number of membrane localized pixels to calculate the average pixel intensity.

719 To isolate Brp pixels that colocalized with DLG, the DLG channel was first thresholded
720 using FIJI's default auto-thresholding function, binarized in MATLAB, and then multiplied to
721 the Brp channel. An ROI mask was then used to restrict Brp analysis to the VPN glomerulus of
722 interest. The total number of Brp positive pixels was then calculated and the overall volume of
723 Brp-DLG colocalization computed by multiplying the total pixel count by the image voxel size.

724 To quantify LPLC2 glomerulus volume, the LPLC2-membrane channel and Brp channel
725 were thresholded in Fiji and binarized using MATLAB as described above. The two channels
726 were then multiplied where pixels containing both membrane label and Brp were considered part
727 of the glomerulus. Glomerulus volume was determined by multiplying the total glomerulus pixel
728 count by image voxel size.

729 For analyses where dendrite complexity and extension were quantified (Figure 2B,C), a
730 median filter was used to remove background noise. For all other images, no pre-processing was
731 performed, and only the brightness and contrast were adjusted to highlight neuronal processes
732 when preparing images for figure generation. For all data sets using the GF-LexA driver line,
733 any images that had non-GF cell types within our ROI and low or no GF expression because of
734 driver line stochasticity were excluded from analyses.

735

736 **Creation of the LexAop2-Brp-Short-GFP-HSV Transgenic Line**

737 To create a transgenic line expressing Brp-Short-GFP under control of the lexAop
738 promoter (lexAop-Brp-Short-GFP), we used the Gateway cloning system (Thermo Fisher
739 Scientific, cat. No. K202020) via an existing plasmid containing the UAS-Brp-Short sequence¹⁰¹
740 followed by a Gateway cassette. We excised the UAS sequence using dual HindIII and PspXI
741 restriction digests and replaced the promoter with a lexAoperon sequence, flanked by HindIII and
742 PspXI restriction sites, that was first PCR amplified using custom primers (see Table 2) from a
743 plasmid containing lexAop2 (lexAop2-myr-4xSNAPf, RRID: Addgene 87638) and then
744 restriction digested using HindIII and PspXI (New England BioLabs, Ipswich, MA) to create
745 compatible sticky ends. Following ligation and confirmation of the appropriate promoter insertion
746 by sequencing, we replaced the Gateway cassette with the GFP-HSV tag from an Entry vector via

747 Gateway LR recombination reaction (Thermo Fisher Scientific, cat. no. 11791019). Plasmid
748 identity and the presence of all components was verified by sequencing (GeneWiz, South
749 Plainfield, NJ). Transgenic lines of the resultant plasmid inserted into the ϕ C31 site at attP2
750 (Bloomington Drosophila Stock Center, RRID: 8622) located at 68A4 on the 3rd chromosome were
751 then produced using standard methods (BestGene, Inc., Chino Hills, CA). Subsequent lines were
752 verified by genomic sequencing and a single line chosen for experiments.

753

754 **Kir2.1 cell death and GF dendrite localization**

755 To quantify LC4 cell death following early expression of Kir2.1, immunohistochemistry
756 was performed against a GFP conjugated to Kir2.1 or GFP (controls), and Brp. Following
757 imaging, LC4 cell bodies were manually counted using the GFP channel. To quantify GF
758 dendrite density within the LPLC2 glomerulus following LC4 cell death, the Brp channel was
759 used to visualize the optic glomeruli active zones. Axons that make up each individual
760 glomerulus reliably terminate in the same region of the central brain, allowing for consistent
761 identification of the LPLC2 glomerulus.

762

763 **scRNA-seq data analysis**

764 To quantify changes in mRNA expression over development for our cells of interest, a
765 recently published scRNA-seq dataset was used²². For each developmental stage for each
766 population, an unpaired non-parametric Kruskal-Wallis test by ranks was performed, followed
767 by a Dunn-Bonferroni multiple comparisons test for significant groups.

768

769 **Electrophysiology**

770 For adult whole-cell electrophysiology, female flies were head fixed to recording plates
771 via UV glue, antenna were UV-glued, and the front legs were removed at the level of the femur
772 as described previously^{6,63}. GFP positive GF soma were accessed for recordings by removing the
773 cuticle and overlying trachea, and then removing the perineural sheath by local application of
774 collagenase (0.5% in extracellular saline). Brains were perfused with standard extracellular
775 saline (103 mM NaCl, 3 mM KCl, 5 mM *N*-Tris (hydroxymethyl)methyl-2- aminoethane-
776 sulfonic acid, 8 mM trehalose, 10 mM glucose, 26 mM NaHCO₃, 1 mM NaH₂PO₄, 1.5 mM
777 CaCl₂ and 4 mM MgCl₂, pH 7.3, 270–275), bubbled with 95% O₂/5% CO₂ and held at
778 22°C. Recording electrodes (3.5–6.2 MΩ) were filled with intracellular saline (140 mM
779 potassium aspartate, 10 mM HEPES, 1 mM EGTA, 4 mM MgATP, 0.5 mM Na₃GTP, 1 mM
780 KCl, 20 μM Alexa-568-hydrazide-Na, 260–275 mOsm, pH 7.3). Recordings were acquired in
781 whole-cell, current clamp mode, digitized at 20kHz, and low pass filtered at 10kHz. All data
782 were collected using Wavesurfer, an open-source software ([https://www.janelia.org/open-](https://www.janelia.org/open-science/wavesurfer)
783 [science/wavesurfer](https://www.janelia.org/open-science/wavesurfer)) running in MATLAB. Recordings were deemed acceptable if a high seal
784 was attained prior to break through, the resting membrane potential was ≤ -55 mV, and the input
785 resistance was > 50 MΩ. Current was not injected to hold the membrane potential at a particular
786 resting level, and traces were not corrected for a 13mV liquid junction potential¹⁰².

787 All pupal recordings were staged in accordance with our staging protocol. Extracellular
788 and intracellular reagents used were identical to the reagents used for adult recordings.
789 Recordings were acquired in whole-cell, current clamp mode, digitized at 20kHz, and low pass
790 filtered at 10kHz. All data were collected using Wavesurfer running in MATLAB. Recordings
791 were deemed acceptable if recording electrodes (3.4 – 5.2 MΩ) attained a high seal (GΩ range)
792 prior to break through, the resting membrane potential was below -30mV and remained stable

793 throughout the duration of the recording, and the input resistance ranged from 50 M Ω to 300
794 M Ω . Current was not injected to hold the membrane potential at a particular resting level, and
795 traces were not corrected for a 13mV liquid junction potential¹⁰².

796

797 **Optogenetics**

798 Light activation of VPN cell types expressing CsChrimson⁹⁷ while recording from GF
799 was performed by delivering light (635nm LED, Scientifica) through a 40x objective focused on
800 a head fixed fly. Light pulses (5ms, 1.7 μ W/mm², as measured in air at the working distance of
801 the objective) were delivered 5 times at 30 second intervals.

802

803 **Visual Stimuli**

804 Visual stimuli were projected on a cylindrical screen surrounding a head fixed fly during
805 whole-cell electrophysiology following the protocol described previously^{63,103}. A 4.5-inch
806 diameter mylar cylindrical screen covered 180° in azimuth, and two DLP projectors (Texas
807 Instruments Lightcrafter 4500) were used to minimize luminance attenuation at the end of the
808 screen edge. The projections from the two projectors were calibrated on the cylindrical screen
809 surface as described previously¹⁰³ and the two projections overlapped 18° in azimuth at center of
810 the screen and blended for uniform illumination. Generated looming stimuli based on the
811 equation¹⁰⁴ below and constant velocity expansion stimuli were displayed with 912 x 1140
812 resolution in 6bit grayscale at 240 Hz which is above the flicker fusion frequency of *Drosophila*
813 (100 Hz¹⁰⁵). Looming stimuli were generated by simulating a 2D projection of an object
814 approaching at a constant velocity which mimics an approaching predator. The angular size (θ)

815 of the stimulus subtended by the approaching object and was calculated over time (t) by the
816 following equation¹⁰⁴:

$$817 \quad \theta(t) = 2 \tan^{-1} \left(\frac{r}{vt} \right)$$

818 where $t < 0$ before collision and $t = 0$ at collision for an approaching object with a half size (r) and
819 constant velocity (v). Four looming stimuli ($r/v = 10, 20, 40, 80$ ms) were displayed, starting at
820 10° , expanding to 63° and then held for 1 second. Stimuli were presented once per trial, in a
821 randomized order, every 30 seconds. For each fly, two trials of the entire set of stimuli were
822 averaged.

823

824 **Data analysis and Statistics**

825 No power analysis was performed prior to statistical analysis. Volume analysis in Figure
826 3 was performed by a researcher blinded to the genotypes. All data from confocal microscopy
827 experiments were tested for normality using a Kolmogorov-Smirnov test or Anderson-Darling
828 test and the appropriate parametric or non-parametric test was performed, as stated in the figure
829 captions.

830 For boxplots, the dividing line in the box indicates the median, the boxes contain the
831 interquartile range, and the whiskers indicate the extent of data points within an additional
832 $1.5 \times$ interquartile range.

833 For *in-vivo* electrophysiology analyses in adult recordings, all analyses were performed
834 using custom MATLAB scripts. Recordings for each stimulus presentation were baseline
835 subtracted by taking the average response one second prior to the stimulus onset. The magnitude
836 of the GF expansion peak was measured after filtering each recording (Savitzky–Golay, fourth
837 order polynomial, frame size is 1/10th the length of the stimulus). The normality of the data was

838 assessed using a Kolmogorov-Smirnov test. If the data were found to not follow a normal
839 distribution, the appropriate non-parametric test was selected. For non-parametric analyses, a
840 Kruskal-Wallis test was performed, and Tukey-Kramer post hoc test was performed for
841 significant groups.

842 For *ex-plant* pupal recordings, all analyses were performed using in-house MATLAB
843 scripts. Potential 60Hz noise was filtered out using a band-stop filter, and thirty minutes of data
844 were quantified. The baseline was determined after two rounds of computing the average signal
845 envelope. Peaks were identified by capturing all depolarizations that were 3mV above baseline
846 and separated by at least 100ms. Time intervals between events were transformed into
847 instantaneous frequency for histogram plots.

848

849

850

851

852

853

854

855

856

857

858

859

860

861

862

863 REFERENCES

- 864 1 Di Martino, A. *et al.* Unraveling the miswired connectome: a developmental perspective.
865 *Neuron* **83**, 1335-1353, doi:10.1016/j.neuron.2014.08.050 (2014).
- 866 2 Zuo, X. N. Editorial: Mapping the Miswired Connectome in Autism Spectrum Disorder.
867 *J Am Acad Child Adolesc Psychiatry* **59**, 348-349, doi:10.1016/j.jaac.2020.01.001 (2020).
- 868 3 Xie, Y. *et al.* Alterations in Connectome Dynamics in Autism Spectrum Disorder: A
869 Harmonized Mega- and Meta-analysis Study Using the Autism Brain Imaging Data
870 Exchange Dataset. *Biol Psychiatry* **91**, 945-955, doi:10.1016/j.biopsych.2021.12.004
871 (2022).
- 872 4 Johnston, M. V. *et al.* Plasticity and injury in the developing brain. *Brain Dev* **31**, 1-10,
873 doi:10.1016/j.braindev.2008.03.014 (2009).
- 874 5 Newport, E. L. *et al.* Language and developmental plasticity after perinatal stroke. *Proc*
875 *Natl Acad Sci U S A* **119**, e2207293119, doi:10.1073/pnas.2207293119 (2022).
- 876 6 von Reyn, C. R. *et al.* Feature Integration Drives Probabilistic Behavior in the Drosophila
877 Escape Response. *Neuron* **94**, 1190-1204 e1196, doi:10.1016/j.neuron.2017.05.036
878 (2017).
- 879 7 Ache, J. M. *et al.* Neural Basis for Looming Size and Velocity Encoding in the
880 Drosophila Giant Fiber Escape Pathway. *Curr Biol* **29**, 1073-1081 e1074,
881 doi:10.1016/j.cub.2019.01.079 (2019).
- 882 8 Morimoto, M. M. *et al.* Spatial readout of visual looming in the central brain of
883 Drosophila. *Elife* **9**, doi:10.7554/eLife.57685 (2020).
- 884 9 Klapoetke, N. C. *et al.* A functionally ordered visual feature map in the Drosophila brain.
885 *Neuron* **110**, 1700-1711 e1706, doi:10.1016/j.neuron.2022.02.013 (2022).
- 886 10 Dombrowski, M. *et al.* Synaptic gradients transform object location to action. *Nature* **613**,
887 534-542, doi:10.1038/s41586-022-05562-8 (2023).
- 888 11 Wu, M. *et al.* Visual projection neurons in the Drosophila lobula link feature detection to
889 distinct behavioral programs. *Elife* **5**, doi:10.7554/eLife.21022 (2016).
- 890 12 Keles, M. & Frye, M. A. The eyes have it. *Elife* **6**, doi:10.7554/eLife.24896 (2017).
- 891 13 Klapoetke, N. C. *et al.* Ultra-selective looming detection from radial motion opponency.
892 *Nature* **551**, 237-241, doi:10.1038/nature24626 (2017).
- 893 14 Ribeiro, I. M. A. *et al.* Visual Projection Neurons Mediating Directed Courtship in
894 Drosophila. *Cell* **174**, 607-621 e618, doi:10.1016/j.cell.2018.06.020 (2018).
- 895 15 Hsu, C. T. & Bhandawat, V. Organization of descending neurons in Drosophila
896 melanogaster. *Sci Rep* **6**, 20259, doi:10.1038/srep20259 (2016).
- 897 16 Namiki, S., Dickinson, M. H., Wong, A. M., Korff, W. & Card, G. M. The functional
898 organization of descending sensory-motor pathways in Drosophila. *Elife* **7**,
899 doi:10.7554/eLife.34272 (2018).
- 900 17 von Reyn, C. R. *et al.* A spike-timing mechanism for action selection. *Nat Neurosci* **17**,
901 962-970, doi:10.1038/nn.3741 (2014).
- 902 18 Wilson, R. I. Early olfactory processing in Drosophila: mechanisms and principles. *Annu*
903 *Rev Neurosci* **36**, 217-241, doi:10.1146/annurev-neuro-062111-150533 (2013).

- 904 19 Peek, M. Y. *Control of Escape Behavior by Descending Neurons in Drosophila*
905 *Melanogaster*, The University of Chicago, (2018).
- 906 20 Zheng, Z. *et al.* A Complete Electron Microscopy Volume of the Brain of Adult
907 *Drosophila melanogaster*. *Cell* **174**, 730-743 e722, doi:10.1016/j.cell.2018.06.019 (2018).
- 908 21 Scheffer, L. K. *et al.* A connectome and analysis of the adult *Drosophila* central brain.
909 *Elife* **9**, doi:10.7554/eLife.57443 (2020).
- 910 22 Kurmangaliyev, Y. Z., Yoo, J., Valdes-Aleman, J., Sanfilippo, P. & Zipursky, S. L.
911 Transcriptional Programs of Circuit Assembly in the *Drosophila* Visual System. *Neuron*
912 **108**, 1045-1057 e1046, doi:10.1016/j.neuron.2020.10.006 (2020).
- 913 23 Clements, J. C. neuPrint: Analysis Tools for EM Connectomics. *BioRxiv* (2020).
- 914 24 Tirian, L. & Dickson, B. J. The VT GAL4, LexA, and split-GAL4 driver line collections
915 for targeted expression in the *Drosophila* nervous system. *bioRxiv*, 198648,
916 doi:10.1101/198648 (2017).
- 917 25 Gordon, M. D. & Scott, K. Motor control in a *Drosophila* taste circuit. *Neuron* **61**, 373-
918 384, doi:10.1016/j.neuron.2008.12.033 (2009).
- 919 26 Feinberg, E. H. *et al.* GFP Reconstitution Across Synaptic Partners (GRASP) defines cell
920 contacts and synapses in living nervous systems. *Neuron* **57**, 353-363,
921 doi:10.1016/j.neuron.2007.11.030 (2008).
- 922 27 Allen, M. J., Drummond, J. A. & Moffat, K. G. Development of the giant fiber neuron of
923 *Drosophila melanogaster*. *J Comp Neurol* **397**, 519-531, doi:10.1002/(sici)1096-
924 9861(19980810)397:4<519::aid-cne5>3.0.co;2-4 (1998).
- 925 28 Jacobs, K., Todman, M. G., Allen, M. J., Davies, J. A. & Bacon, J. P. Synaptogenesis in
926 the giant-fibre system of *Drosophila*: interaction of the giant fibre and its major
927 motoneuronal target. *Development* **127**, 5203-5212, doi:10.1242/dev.127.23.5203
928 (2000).
- 929 29 Godenschwege, T. A., Hu, H., Shan-Crofts, X., Goodman, C. S. & Murphey, R. K. Bi-
930 directional signaling by Semaphorin 1a during central synapse formation in *Drosophila*.
931 *Nat Neurosci* **5**, 1294-1301, doi:10.1038/nn976 (2002).
- 932 30 Murphey, R. K. *et al.* Targeted expression of shibire ts and semaphorin 1a reveals critical
933 periods for synapse formation in the giant fiber of *Drosophila*. *Development* **130**, 3671-
934 3682, doi:10.1242/dev.00598 (2003).
- 935 31 Allen, M. J., Godenschwege, T. A., Tanouye, M. A. & Phelan, P. Making an escape:
936 development and function of the *Drosophila* giant fibre system. *Semin Cell Dev Biol* **17**,
937 31-41, doi:10.1016/j.semcdb.2005.11.011 (2006).
- 938 32 Kennedy, T. & Brodie, K. Newly Identified Electrically Coupled Neurons Support
939 Development of the *Drosophila* Giant Fiber Model Circuit. *eNeuro* **5**,
940 doi:10.1523/ENEURO.0346-18.2018 (2018).
- 941 33 Phelan, P. *et al.* Molecular mechanism of rectification at identified electrical synapses in
942 the *Drosophila* giant fiber system. *Curr Biol* **18**, 1955-1960,
943 doi:10.1016/j.cub.2008.10.067 (2008).
- 944 34 Courgeon, M. & Desplan, C. Coordination of neural patterning in the *Drosophila* visual
945 system. *Curr Opin Neurobiol* **56**, 153-159, doi:10.1016/j.conb.2019.01.024 (2019).
- 946 35 Mora, N. *et al.* A Temporal Transcriptional Switch Governs Stem Cell Division,
947 Neuronal Numbers, and Maintenance of Differentiation. *Dev Cell* **45**, 53-66 e55,
948 doi:10.1016/j.devcel.2018.02.023 (2018).

- 949 36 Apitz, H. & Salecker, I. A region-specific neurogenesis mode requires migratory
950 progenitors in the Drosophila visual system. *Nat Neurosci* **18**, 46-55,
951 doi:10.1038/nn.3896 (2015).
- 952 37 Pinto-Teixeira, F. *et al.* Development of Concurrent Retinotopic Maps in the Fly Motion
953 Detection Circuit. *Cell* **173**, 485-498 e411, doi:10.1016/j.cell.2018.02.053 (2018).
- 954 38 Shearin, H. K., Quinn, C. D., Mackin, R. D., Macdonald, I. S. & Stowers, R. S. t-
955 GRASP, a targeted GRASP for assessing neuronal connectivity. *J Neurosci Methods* **306**,
956 94-102, doi:10.1016/j.jneumeth.2018.05.014 (2018).
- 957 39 Wagh, D. A. *et al.* Bruchpilot, a protein with homology to ELKS/CAST, is required for
958 structural integrity and function of synaptic active zones in Drosophila. *Neuron* **49**, 833-
959 844, doi:10.1016/j.neuron.2006.02.008 (2006).
- 960 40 Knapek, S., Sigrist, S. & Tanimoto, H. Bruchpilot, a synaptic active zone protein for
961 anesthesia-resistant memory. *J Neurosci* **31**, 3453-3458, doi:10.1523/JNEUROSCI.2585-
962 10.2011 (2011).
- 963 41 Megighian, A. *et al.* Evidence for a radial SNARE super-complex mediating
964 neurotransmitter release at the Drosophila neuromuscular junction. *J Cell Sci* **126**, 3134-
965 3140, doi:10.1242/jcs.123802 (2013).
- 966 42 Cho, R. W., Song, Y. & Littleton, J. T. Comparative analysis of Drosophila and
967 mammalian complexins as fusion clamps and facilitators of neurotransmitter release. *Mol*
968 *Cell Neurosci* **45**, 389-397, doi:10.1016/j.mcn.2010.07.012 (2010).
- 969 43 Scholz, N. *et al.* Complexin cooperates with Bruchpilot to tether synaptic vesicles to the
970 active zone cytomatrix. *J Cell Biol* **218**, 1011-1026, doi:10.1083/jcb.201806155 (2019).
- 971 44 Davis, F. P. *et al.* A genetic, genomic, and computational resource for exploring neural
972 circuit function. *Elife* **9**, doi:10.7554/eLife.50901 (2020).
- 973 45 Buccitelli, C. & Selbach, M. mRNAs, proteins and the emerging principles of gene
974 expression control. *Nat Rev Genet* **21**, 630-644, doi:10.1038/s41576-020-0258-4 (2020).
- 975 46 Peng, J. *et al.* Drosophila Fezf coordinates laminar-specific connectivity through cell-
976 intrinsic and cell-extrinsic mechanisms. *Elife* **7**, doi:10.7554/eLife.33962 (2018).
- 977 47 Fouquet, W. *et al.* Maturation of active zone assembly by Drosophila Bruchpilot. *J Cell*
978 *Biol* **186**, 129-145, doi:10.1083/jcb.200812150 (2009).
- 979 48 Duhart, J. C. & Mosca, T. J. Genetic regulation of central synapse formation and
980 organization in Drosophila melanogaster. *Genetics* **221**, doi:10.1093/genetics/iyac078
981 (2022).
- 982 49 Parisi, M. J., Aimino, M. A. & Mosca, T. J. A conditional strategy for cell-type-specific
983 labeling of endogenous excitatory synapses in Drosophila. *Cell Reports Methods* **3**,
984 100477, doi:https://doi.org/10.1016/j.crmeth.2023.100477 (2023).
- 985 50 Woods, D. F. & Bryant, P. J. The discs-large tumor suppressor gene of Drosophila
986 encodes a guanylate kinase homolog localized at septate junctions. *Cell* **66**, 451-464,
987 doi:10.1016/0092-8674(81)90009-x (1991).
- 988 51 Akin, O., Bajar, B. T., Keles, M. F., Frye, M. A. & Zipursky, S. L. Cell-type-Specific
989 Patterned Stimulus-Independent Neuronal Activity in the Drosophila Visual System
990 during Synapse Formation. *Neuron* **101**, 894-904 e895,
991 doi:10.1016/j.neuron.2019.01.008 (2019).
- 992 52 Bajar, B. T. *et al.* A discrete neuronal population coordinates brain-wide developmental
993 activity. *Nature* **602**, 639-646, doi:10.1038/s41586-022-04406-9 (2022).

- 994 53 Wong, R. O., Meister, M. & Shatz, C. J. Transient period of correlated bursting activity
995 during development of the mammalian retina. *Neuron* **11**, 923-938, doi:10.1016/0896-
996 6273(93)90122-8 (1993).
- 997 54 Moreno-Juan, V. *et al.* Prenatal thalamic waves regulate cortical area size prior to sensory
998 processing. *Nat Commun* **8**, 14172, doi:10.1038/ncomms14172 (2017).
- 999 55 D'Souza, S. & Lang, R. A. Retinal ganglion cell interactions shape the developing
1000 mammalian visual system. *Development* **147**, doi:10.1242/dev.196535 (2020).
- 1001 56 Ackman, J. B., Burbridge, T. J. & Crair, M. C. Retinal waves coordinate patterned
1002 activity throughout the developing visual system. *Nature* **490**, 219-225,
1003 doi:10.1038/nature11529 (2012).
- 1004 57 Spitzer, N. C. Electrical activity in early neuronal development. *Nature* **444**, 707-712,
1005 doi:10.1038/nature05300 (2006).
- 1006 58 Pfeiffer, B. D., Truman, J. W. & Rubin, G. M. Using translational enhancers to increase
1007 transgene expression in Drosophila. *Proc Natl Acad Sci U S A* **109**, 6626-6631,
1008 doi:10.1073/pnas.1204520109 (2012).
- 1009 59 Harrell, E. R., Pimentel, D. & Miesenbock, G. Changes in Presynaptic Gene Expression
1010 during Homeostatic Compensation at a Central Synapse. *J Neurosci* **41**, 3054-3067,
1011 doi:10.1523/JNEUROSCI.2979-20.2021 (2021).
- 1012 60 Yamazaki, D. *et al.* Contribution of K(ir)2 potassium channels to ATP-induced cell death
1013 in brain capillary endothelial cells and reconstructed HEK293 cell model. *Am J Physiol*
1014 *Cell Physiol* **300**, C75-86, doi:10.1152/ajpcell.00135.2010 (2011).
- 1015 61 Desai, N. S., Rutherford, L. C. & Turrigiano, G. G. Plasticity in the intrinsic excitability
1016 of cortical pyramidal neurons. *Nat Neurosci* **2**, 515-520, doi:10.1038/9165 (1999).
- 1017 62 Pecot, M. Y. *et al.* Sequential axon-derived signals couple target survival and layer
1018 specificity in the Drosophila visual system. *Neuron* **82**, 320-333,
1019 doi:10.1016/j.neuron.2014.02.045 (2014).
- 1020 63 Jang, H., Goodman, D. P., Ausborn, J. & von Reyn, C. R. Azimuthal invariance to
1021 looming stimuli in the Drosophila giant fiber escape circuit. *J Exp Biol* **226**,
1022 doi:10.1242/jeb.244790 (2023).
- 1023 64 Joesch, M., Schnell, B., Raghu, S. V., Reiff, D. F. & Borst, A. ON and OFF pathways in
1024 Drosophila motion vision. *Nature* **468**, 300-304, doi:10.1038/nature09545 (2010).
- 1025 65 Tuthill, J. C., Nern, A., Holtz, S. L., Rubin, G. M. & Reiser, M. B. Contributions of the
1026 12 neuron classes in the fly lamina to motion vision. *Neuron* **79**, 128-140,
1027 doi:10.1016/j.neuron.2013.05.024 (2013).
- 1028 66 Kolodkin, A. L. & Hiesinger, P. R. Wiring visual systems: common and divergent
1029 mechanisms and principles. *Curr Opin Neurobiol* **42**, 128-135,
1030 doi:10.1016/j.conb.2016.12.006 (2017).
- 1031 67 Li, T. *et al.* Cellular bases of olfactory circuit assembly revealed by systematic time-lapse
1032 imaging. *Cell* **184**, 5107-5121 e5114, doi:10.1016/j.cell.2021.08.030 (2021).
- 1033 68 Sanes, J. R. & Zipursky, S. L. Synaptic Specificity, Recognition Molecules, and
1034 Assembly of Neural Circuits. *Cell* **181**, 1434-1435, doi:10.1016/j.cell.2020.05.046
1035 (2020).
- 1036 69 Luhmann, H. J. & Khazipov, R. Neuronal activity patterns in the developing barrel
1037 cortex. *Neuroscience* **368**, 256-267, doi:10.1016/j.neuroscience.2017.05.025 (2018).

- 1038 70 Choi, B. J., Chen, Y. D. & Desplan, C. Building a circuit through correlated spontaneous
1039 neuronal activity in the developing vertebrate and invertebrate visual systems. *Genes Dev*
1040 **35**, 677-691, doi:10.1101/gad.348241.121 (2021).
- 1041 71 Kutsarova, E., Munz, M. & Ruthazer, E. S. Rules for Shaping Neural Connections in the
1042 Developing Brain. *Front Neural Circuits* **10**, 111, doi:10.3389/fncir.2016.00111 (2016).
- 1043 72 Dupont, E., Hanganu, I. L., Kilb, W., Hirsch, S. & Luhmann, H. J. Rapid developmental
1044 switch in the mechanisms driving early cortical columnar networks. *Nature* **439**, 79-83,
1045 doi:10.1038/nature04264 (2006).
- 1046 73 Hanganu, I. L., Ben-Ari, Y. & Khazipov, R. Retinal waves trigger spindle bursts in the
1047 neonatal rat visual cortex. *J Neurosci* **26**, 6728-6736, doi:10.1523/JNEUROSCI.0752-
1048 06.2006 (2006).
- 1049 74 Yu, Y. C. *et al.* Preferential electrical coupling regulates neocortical lineage-dependent
1050 microcircuit assembly. *Nature* **486**, 113-117, doi:10.1038/nature10958 (2012).
- 1051 75 Shatz, C. J. Emergence of order in visual system development. *Proc Natl Acad Sci U S A*
1052 **93**, 602-608, doi:10.1073/pnas.93.2.602 (1996).
- 1053 76 Carroll, B. J., Bertram, R. & Hyson, R. L. Intrinsic physiology of inhibitory neurons
1054 changes over auditory development. *J Neurophysiol* **119**, 290-304,
1055 doi:10.1152/jn.00447.2017 (2018).
- 1056 77 Rabinovich, D., Maysel, O. & Schuldiner, O. Long term ex vivo culturing of
1057 *Drosophila* brain as a method to live image pupal brains: insights into the cellular
1058 mechanisms of neuronal remodeling. *Front Cell Neurosci* **9**, 327,
1059 doi:10.3389/fncel.2015.00327 (2015).
- 1060 78 Ozel, M. N., Langen, M., Hassan, B. A. & Hiesinger, P. R. Filopodial dynamics and
1061 growth cone stabilization in *Drosophila* visual circuit development. *Elife* **4**,
1062 doi:10.7554/eLife.10721 (2015).
- 1063 79 Li, T. & Luo, L. An Explant System for Time-Lapse Imaging Studies of Olfactory Circuit
1064 Assembly in *Drosophila*. *J Vis Exp*, doi:10.3791/62983 (2021).
- 1065 80 Spruston, N. Pyramidal neurons: dendritic structure and synaptic integration. *Nat Rev*
1066 *Neurosci* **9**, 206-221, doi:10.1038/nrn2286 (2008).
- 1067 81 Gidon, A. & Segev, I. Principles governing the operation of synaptic inhibition in
1068 dendrites. *Neuron* **75**, 330-341, doi:10.1016/j.neuron.2012.05.015 (2012).
- 1069 82 Ferreira, J. S. *et al.* Distance-dependent regulation of NMDAR nanoscale organization
1070 along hippocampal neuron dendrites. *Proc Natl Acad Sci U S A* **117**, 24526-24533,
1071 doi:10.1073/pnas.1922477117 (2020).
- 1072 83 Jefferis, G. S. *et al.* Developmental origin of wiring specificity in the olfactory system of
1073 *Drosophila*. *Development* **131**, 117-130, doi:10.1242/dev.00896 (2004).
- 1074 84 Berdnik, D., Chihara, T., Couto, A. & Luo, L. Wiring stability of the adult *Drosophila*
1075 olfactory circuit after lesion. *J Neurosci* **26**, 3367-3376, doi:10.1523/JNEUROSCI.4941-
1076 05.2006 (2006).
- 1077 85 Yogeve, S. & Shen, K. Cellular and molecular mechanisms of synaptic specificity. *Annu*
1078 *Rev Cell Dev Biol* **30**, 417-437, doi:10.1146/annurev-cellbio-100913-012953 (2014).
- 1079 86 Sassoe-Pognetto, M. & Patrizi, A. The Purkinje cell as a model of synaptogenesis and
1080 synaptic specificity. *Brain Res Bull* **129**, 12-17, doi:10.1016/j.brainresbull.2016.10.004
1081 (2017).

- 1082 87 Chowdhury, D., Watters, K. & Biederer, T. Synaptic recognition molecules in
1083 development and disease. *Curr Top Dev Biol* **142**, 319-370,
1084 doi:10.1016/bs.ctdb.2020.12.009 (2021).
- 1085 88 Zhou, D. *et al.* AnkyrinG is required for clustering of voltage-gated Na channels at axon
1086 initial segments and for normal action potential firing. *J Cell Biol* **143**, 1295-1304,
1087 doi:10.1083/jcb.143.5.1295 (1998).
- 1088 89 Brachet, A. *et al.* Ankyrin G restricts ion channel diffusion at the axonal initial segment
1089 before the establishment of the diffusion barrier. *J Cell Biol* **191**, 383-395,
1090 doi:10.1083/jcb.201003042 (2010).
- 1091 90 Ango, F. *et al.* Ankyrin-based subcellular gradient of neurofascin, an immunoglobulin
1092 family protein, directs GABAergic innervation at purkinje axon initial segment. *Cell* **119**,
1093 257-272, doi:10.1016/j.cell.2004.10.004 (2004).
- 1094 91 Buttermore, E. D. *et al.* Pinceau organization in the cerebellum requires distinct functions
1095 of neurofascin in Purkinje and basket neurons during postnatal development. *J Neurosci*
1096 **32**, 4724-4742, doi:10.1523/JNEUROSCI.5602-11.2012 (2012).
- 1097 92 Sanes, J. R. & Zipursky, S. L. Design principles of insect and vertebrate visual systems.
1098 *Neuron* **66**, 15-36, doi:10.1016/j.neuron.2010.01.018 (2010).
- 1099 93 Seabrook, T. A., Burbridge, T. J., Crair, M. C. & Huberman, A. D. Architecture,
1100 Function, and Assembly of the Mouse Visual System. *Annu Rev Neurosci* **40**, 499-538,
1101 doi:10.1146/annurev-neuro-071714-033842 (2017).
- 1102 94 Schneider, K. A. & Kastner, S. Visual responses of the human superior colliculus: a high-
1103 resolution functional magnetic resonance imaging study. *J Neurophysiol* **94**, 2491-2503,
1104 doi:10.1152/jn.00288.2005 (2005).
- 1105 95 Pezier, A. P., Jezzini, S. H., Bacon, J. P. & Blagburn, J. M. Shaking B Mediates Synaptic
1106 Coupling between Auditory Sensory Neurons and the Giant Fiber of *Drosophila*
1107 *melanogaster*. *PLoS One* **11**, e0152211, doi:10.1371/journal.pone.0152211 (2016).
- 1108 96 Nern, A., Pfeiffer, B. D. & Rubin, G. M. Optimized tools for multicolor stochastic
1109 labeling reveal diverse stereotyped cell arrangements in the fly visual system. *Proc Natl*
1110 *Acad Sci U S A* **112**, E2967-2976, doi:10.1073/pnas.1506763112 (2015).
- 1111 97 Klapoetke, N. C. *et al.* Independent optical excitation of distinct neural populations. *Nat*
1112 *Methods* **11**, 338-346, doi:10.1038/nmeth.2836 (2014).
- 1113 98 Pfeiffer, B. D. *et al.* Refinement of tools for targeted gene expression in *Drosophila*.
1114 *Genetics* **186**, 735-755, doi:10.1534/genetics.110.119917 (2010).
- 1115 99 Wu, J. S. & Luo, L. A protocol for dissecting *Drosophila melanogaster* brains for live
1116 imaging or immunostaining. *Nat Protoc* **1**, 2110-2115, doi:10.1038/nprot.2006.336
1117 (2006).
- 1118 100 Sweeney, S. T., Broadie, K., Keane, J., Niemann, H. & O'Kane, C. J. Targeted expression
1119 of tetanus toxin light chain in *Drosophila* specifically eliminates synaptic transmission
1120 and causes behavioral defects. *Neuron* **14**, 341-351, doi:10.1016/0896-6273(95)90290-2
1121 (1995).
- 1122 101 Mosca, T. J., Luginbuhl, D. J., Wang, I. E. & Luo, L. Presynaptic LRP4 promotes
1123 synapse number and function of excitatory CNS neurons. *Elife* **6**,
1124 doi:10.7554/eLife.27347 (2017).
- 1125 102 Gouwens, N. W. & Wilson, R. I. Signal propagation in *Drosophila* central neurons. *J*
1126 *Neurosci* **29**, 6239-6249, doi:10.1523/JNEUROSCI.0764-09.2009 (2009).

- 1127 103 Goodman, D. P., Eldredge, A. & von Reyn, C. R. A novel assay to evaluate action
1128 selection in escape behavior. *J Neurosci Methods* **304**, 154-161,
1129 doi:10.1016/j.jneumeth.2018.04.019 (2018).
1130 104 Gabbiani, F., Krapp, H. G. & Laurent, G. Computation of object approach by a wide-
1131 field, motion-sensitive neuron. *J Neurosci* **19**, 1122-1141, doi:10.1523/JNEUROSCI.19-
1132 03-01122.1999 (1999).
1133 105 Niven, J. E. *et al.* The contribution of Shaker K⁺ channels to the information capacity of
1134 *Drosophila* photoreceptors. *Nature* **421**, 630-634, doi:10.1038/nature01384 (2003).
1135

1136 ACKNOWLEDGEMENTS

1137 We thank the Janelia FlyLight project team for assistance with split-GAL4 generation. This
1138 study was supported in part by the National Science Foundation (grant no. IOS-1921065 to
1139 C.R.v.R.), the National Institutes of Health (NINDS R01NS110907 to T.J.M. and NINDS
1140 R01NS118562 to C.R.v.R.) and the Margaret Q. Landenberger Research Foundation (grant to
1141 C.R.v.R.).

1142

1143 AUTHOR CONTRIBUTIONS

1144 Conceptualization C.R.v.R.; Methodology, B.W.M and C.R.v.R.; Investigation, B.W.M., H.J.,
1145 Y.Z.K., N.S., B.W.H. and C.R.v.R. Writing – Original Draft, B.W.M. and C.R.v.R.; Writing –
1146 Review & Editing, B.W.M., N.S., H.J., B.W.H., T.A.G., Y.Z.K., A.N., M.J.P, K.C.D, T.J.M.,
1147 and C.R.v.R.; Funding Acquisition, C.R.v.R.; Resources, M.J.P, K.C.D, T.J.M., T.A.G., Y.Z.K.
1148 and A.N.; Supervision, C.R.v.R.

1149

1150 DECLARATION OF INTERESTS

1151 The authors declare no competing interests.

1152